Eidgenössische Technische Hochschule Zürich
Swiss Federal Institute of Technology Zurich

Generation of Bragg Spectroscopy Potentials with a DMD

Gloria Clausen

ETH Zürich, Physics Department

University of Oxford, Physics Department

Supervisors: Prof. Dr. Tilman Esslinger, Dr. Robert Smith

A thesis submitted for the degree of

Master of Science

May 7, 2020

Abstract

This thesis describes the design and installation of a Bragg spectroscopy setup using a digital micromirror device (DMD). The conducted work involves the generation of translating sinusoidal lattice potentials for erbium atoms via spatial modulation of a laser beam's intensity profile, and the subsequent projection of the sinusoidal pattern using a suitable imaging setup.
For this, we employ the direct projection method using a two-stage demagnification setup, where a custom objective is introduced to account for multiple types of aberrations.The lower resolution bound of our imaging setup is given by the objective's resolution $r_{\text{objective}} = 2.18 \pm 0.19$ µm, with the average resolution of the setup being measured at $r = 2.55 \pm 0.12$ µm over the extent of the atomic cloud.
The quality of the sinusoidal patterns created by the imaging setup was tested and improved using an iterative correction process to account for beam inhomogeneities and aberrations.
Additionally, the switching dynamics of the DMD were investigated. Clean switching between consecutive frames with refresh rates up to 10.3 kHz enabled a smooth spatial translation.
The performed calibrations and measurements are crucial for the successful probing of the dispersion relation of dipolar quantum gases in the roton regime via Bragg spectroscopy.

Contents

1 Introduction

1.1 Overview of Ultracold Atomic Systems

The development of quantum theory in the first part of the 20^{th} century contributed enormously to our current understanding of the microscopic world. While simple few-particle systems can be solved exactly and provide a useful model for several quantum systems, most phenomena in our modern physics require a many-particle description. Due to the lack of experimental implementation options, it has remained a difficult task to understand and exactly solve many-body problems.
The ability to cool down atomic species to quantum degeneracy in combination with tools to manipulate and control the gases (eg. optically or magnetically) provides the necessary conditions for feasible many-body experiments. With the invention of laser cooling, a great window opened in the field of ultracold atoms, leading to the achievement of the first Bose-Einstein condensate (BEC) in 1995 with rubidium atoms [5] and sodium atoms[12]. Since then, the field of ultracold atoms has proven to be very useful in simulating open problems of many-body quantum systems. Following the first experimental realisation of BEC, a number of ground-breaking studies on many-body quantum effects were demonstrated, such as creating vortices in the superfluid phase [31], [30], matter-wave inteference of BECs [6], the creation of an atomic laser [8], and the observation of long range phase coherence [9]. All these measurements rely on the existence of a coherent, macroscopic matter wave in an interacting many-body system.
An important tool for examining the properties of BECs is Bragg scpectroscopy. It was first used for investigating degenerate condensates in 1999 by Stenger et al. [41]. The method employs stimulated two-photon Bragg scattering to allow measurements on the relative occupation of the different momentum states as well as determining the dynamic structure factor. Bragg spectroscopy was also used to measure the excitation spectrum of a BEC of rubidium atoms [40]. The result confirmed the Bogoliubov spectrum well, with a linear phonon regime for low excitation momenta and a parabolic single-particle regime for higher excitation momenta.

1.2 Interactions in Dipolar Quantum Gases

A natural requirement for the study of correlated systems are particle interactions. Next to the contact interaction, which is the most present interaction for conventional quantum gases, the dipole-dipole interaction (DDI) adds interesting features to observe due to its anisotropic and long-range nature. Dipole-dipole interactions occur between dipolar particles. There exist different species that exhibit dipolar properties, such as magnetic atoms, Rydberg atoms, and heteronuclear molecules. Magnetic atoms are the simplest system to consider since they can be more straightforwardly cooled and manipulated and have a longer lifetime. Three magnetic atoms have been cooled to quantum degeneracy: chromium [20], dysprosium [29], and recently erbium [2], all of which made the DDI available for examination in recent years.
The competition between the contact interaction and anisotropic DDI gives rise to interesting effects. The contact interaction is tunable via Feshbach resonances and is normally set to

be repulsive to avoid the condensate collapsing. The dipolar-dipolar interaction however, is anisotropic and changes sign when varying the relative alignment of two dipoles from the attractive head-to-tale configuration to the repulsive side-by-side configuration. Therefore, the relative strength of the two interactions can be changed by employing magnetic fields and thereby tuning the Feshbach resonance, changing the particle density, and by altering the trap geometry.
In 2003, Santos et al. [37] theoretically predicted the so-called *roton-maxon* character of the excitation spectrum of dipolar quantum gases in contrast to the Bogoliubov spectrum found for non-dipolar BECs which interact via the contact interaction only. Rotons are elementary excitations that manifest themselves as a local minimum in the dispersion relation (energy-momentum relation). The roton-maxon behaviour of the dispersion relation is known from condensed matter systems and has previously been observed in superfluid helium. Landau [27] was the first to relate the roton momentum (the momentum where the energy minimum of the excitation spectrum occurs) to the interparticle distance $q_{\mathrm{rot}} = 1/d$. Fig. 1 shows the dispersion relation for a dipolar quantum gas that exhibits the roton-maxon behaviour.

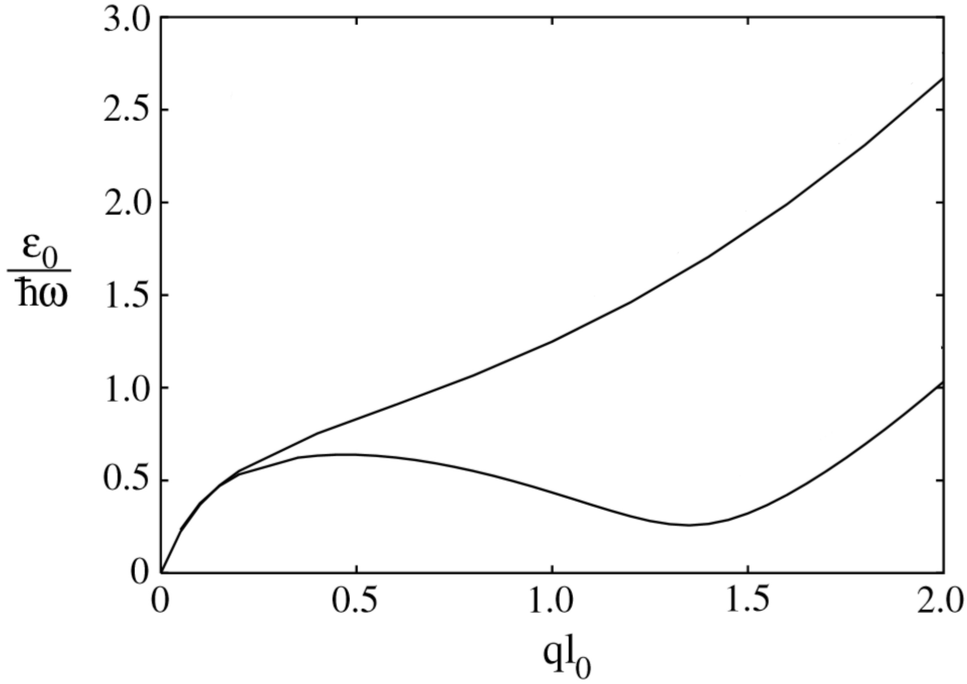

Figure 1: Theoretical excitation spectrum of a dipolar BEC. The top curve shows no roton minimum, as expected for a case where the contact interaction dominates. The bottom curve shows a roton-maxon spectrum and occurs when the dipole-dipole interaction dominates. The minimum is found at $q = 1.4/l_0$, where l_0 is the harmonic oscillator length of the tight confinement motion. The figure is adapted from [37].

Generally, the excitation energy of condensates strongly depends on the interparticle interactions. A dipolar BEC requires a trapping geometry which has a strong confinement in at least one spatial direction (pancake or cigar shaped traps) because in case of no confinement, a head-to-tail configuration of dipoles would lead to a collapse of the condensate due to attractive DDI. Santos et al. [37] showed that in a dipolar BEC trapped in a pancake geometry, the dipole-dipole interaction strength has a special q-dependence. Momenta q that favour an attractive dipole-dipole interaction lead to a minimum in the excitation spectrum. The roton minimum of dipolar BECs is given by $q_{\mathrm{rot}} \approx 1/l_z$, with $l_z = \left(\frac{\hbar}{m\omega_z}\right)^{0.5}$ being the harmonic oscillator length for the tightly confined motion and ω_z the trapping frequency of the confined trapping direction.

Chomaz et al. [11] observed the first spontaneous occupation of the roton mode of condensed erbium in 2017 by tuning the relative strength of contact to dipole-dipole interactions and thereby reducing the roton excitation energy to zero. Two years later, Petter et al. [33] measured the excitation spectrum of condensated erbium using Bragg spectroscopy. They found the relation between the relative strength of contact and dipole-dipole interaction to the magnitude of the roton dip. They also found a stability condition for a dipolar BEC. Both experiments were conducted with a cigar-shaped trapping geometry.

This thesis describes the preparation of a Bragg spectroscopy setup in order to measure the excitation spectrum of condensed erbium in a homogenous quasi 2D-trap, thus enabling us to confirm the theoretical predictions of Santos et al. [37]. The challenge of exciting rotons in a quasi 2D trap is yet to be mastered and will give insight into the physics of radial rotons. Moreover, these measurements will be combined with critical velocity measurements of the condensate and BEC transition temperature measurements.

The Bragg spectroscopy setup will be prepared and tested on a separate setup before being implemented with the erbium experiment. A digital-micromirror device (DMD) is used to generate the Bragg potential which is projected to the atoms using a demagnifying imaging system.

In chapter 2, we will present an overview of the erbium atom and the current status of the erbium experiment in Oxford. Chapter 3 gives an outline of practical requirements for performing Bragg spectroscopy with a DMD. It also shows the theoretical foundations for the Bragg spectroscopy principle and the optical imaging system. Chapter 4 introduces the imaging setup and measurements of its resolution. In chapter 5, we explain how the patterns are binarised and improved using two algorithms. Moreover, the resulting measurements of different optimised patterns are presented. Chapter 6 explains the different operational modes of the DMD. This is supplemented by the results of the switching dynamics measurements using the two operational modes. Lastly, we conclude the thesis in chapter 7, where we summarise the results and give an outlook to the next steps on the route to measuring the dispersion relation of erbium.

2 Cold Atom Machine

2.1 Properties of Erbium

Our experiment investigates the properties of an ultracold sample of erbium atoms. Erbium, a rare-earth atom, is part of the lanthanide series and has the atomic number 68. In this experiment, the second most abundant isotope of erbium is used, ^{168}Er. It is one of five bosonic isotopes of erbium, and there exists one additional fermionic isotope [13]. Among other elements in the lanthanide series, erbium possesses one of the strongest magnetic dipole moments of 7 μ_B. The high magnetic dipole moment results from its electronic structure, where the electronic configuration is given by

$$[\mathrm{Xe}]4f^{12}6s^2,$$

and [Xe] denotes the electronic configuration of xenon. The electrons in the $4f$ shell lead to a total electron spin of $S = 1$ and orbital angular momentum of $L = 6$, resulting in $J = 6$ and the term symbol

$$^3\mathrm{H}_6.$$

Its high magnetic dipole moment in combination with the high number of natural isotopes makes erbium an attractive element for the investigation of long-range dipole-dipole interactions (DDI).

2.2 Laser Cooling Process

We will examine the experimental route to generate a cold sample of erbium atoms in more detail in this chapter. More information on this experiment can be found in the first year reports of Milan Krstajić [26] and Péter Juhász [23].

The experiment is conducted in a vacuum chamber that consists of two parts which are separated by a gate valve. In the experiment, a hot beam of gaseous erbium is created in the "high vacuum chamber" with subsequent transversal cooling before it enters the "ultra-high vacuum chamber" where it undergoes Zeeman slowing and finally will be captured in a magneto-optical trap (MOT). Fig. 2 shows the vacuum chamber including the different laser cooling steps, and Fig. 3 shows a photograph of the vacuum system and the oven.

Erbium exhibits a complex energy structure with many allowed electric-dipole transitions due to its two-electron vacancy in the $4f$ shell. The two major electric-dipole transitions used for laser cooling are the 401 nm and the 583 nm line. The 401 nm line has a natural linewidth of $\Delta\nu$= 29.7 MHz and is more than 150 times bigger than that of the 583 nm line ($\Delta\nu$= 190 kHz), see [22]. Therefore, the 401 nm line is used for the transversal cooling and Zeeman slowing, whereas the 583 nm line is used for the MOT and the Bragg spectroscopy [7].

Atomic erbium is solid at room temperature [14], so we make use of a high-temperature effusion oven to heat the sample to 1200°. As a result, an atomic vapour of erbium atoms is loaded into the vacuum system. The velocity distribution of the hot sample has a maximum at $v_{max} = \sqrt{\frac{3k_B T}{m}} = 465$ m/s.

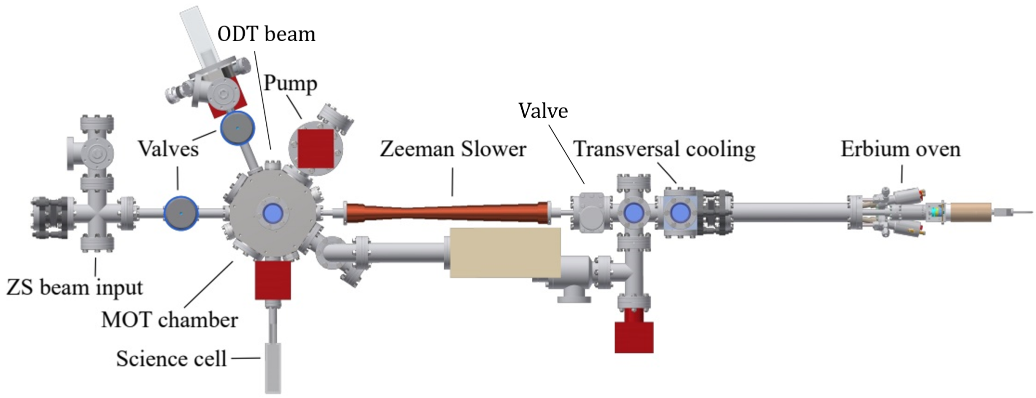

Figure 2: Top view of the experimental vacuum chamber. The left part shows the ultra high vacuum section, which is separated from the high vacuum section on the right by a valve. Atoms enter the setup from the erbium oven and are transversally cooled before entering the ultra high vacuum section. Additional longitudinal cooling in the Zeeman slower prepares them for capturing in the MOT chamber. Then the atoms are loaded into the ODT and transported into the science chamber for evaporation. The figure is adapted from [23].

The first cooling step is reducing the transversal velocity spread of the atomic beam to allow the atoms to pass the valve in a collimated beam and increase the loading effiency into the ultra high vaccum section. The transversal cooling is achieved through the scattering light force exerted by two pairs of counter-propagating 401 nm laser beams. The beams are intersecting the atomic beam orthogonally and are aligned at right angles to each other.
Next, the collimated beam enters the second vacuum section and the Zeeman slower, where cooling in the longitudinal direction slows the atoms down to about 30 m/s. A Zeeman slower cools the atomic beam via momentum transfer through scattering off a collinear, counter-propagating 401 nm laser beam. For the Zeeman slowing process however, an additional spatially-dependent magnetic bias field is required to shift the atomic transition constantly back to resonance using the Zeeman effect. This is necessary because the Doppler shift induces an increasing detuning from resonance when decreasing the atomic velocity.
After exiting the Zeeman slower, the atoms are loaded into a narrow-linewidth MOT. The capture velocity of our MOT cuts off at 10 m/s [17], but further cooling in the Zeeman slower would lead to significant atom losses in the transversal direction. The parameters of Zeeman slowing and MOT loading are tuned to maximise the MOT loading effiency.
The MOT is placed in the MOT chamber in the center of the ultra-high vaccum chamber. It is made up of three pairs of counter-propagating 583 nm laser beams paired with a uniform magnetic gradient field, which is generated by a pair of coils in anti-Helmholtz configuration. This results in an effective force pointing towards the center of the MOT and thus enables cooling and trapping in parallel.
After loading the MOT, it is compressed to the cMOT stage by decreasing the beam power and detuning. MOT cooling on the 583 nm transition would in principle enable temperatures as low as the Doppler limit, given by $T_D = \frac{\hbar\Gamma}{2k_B} = 4.6\ \mu\mathrm{K}$ [28]. The final temperatures reached in the cMOT are around 30 μK, which is significantly higher than the Doppler limit. This is probably due to the frequency fluctuations of the 583 nm laser beam.

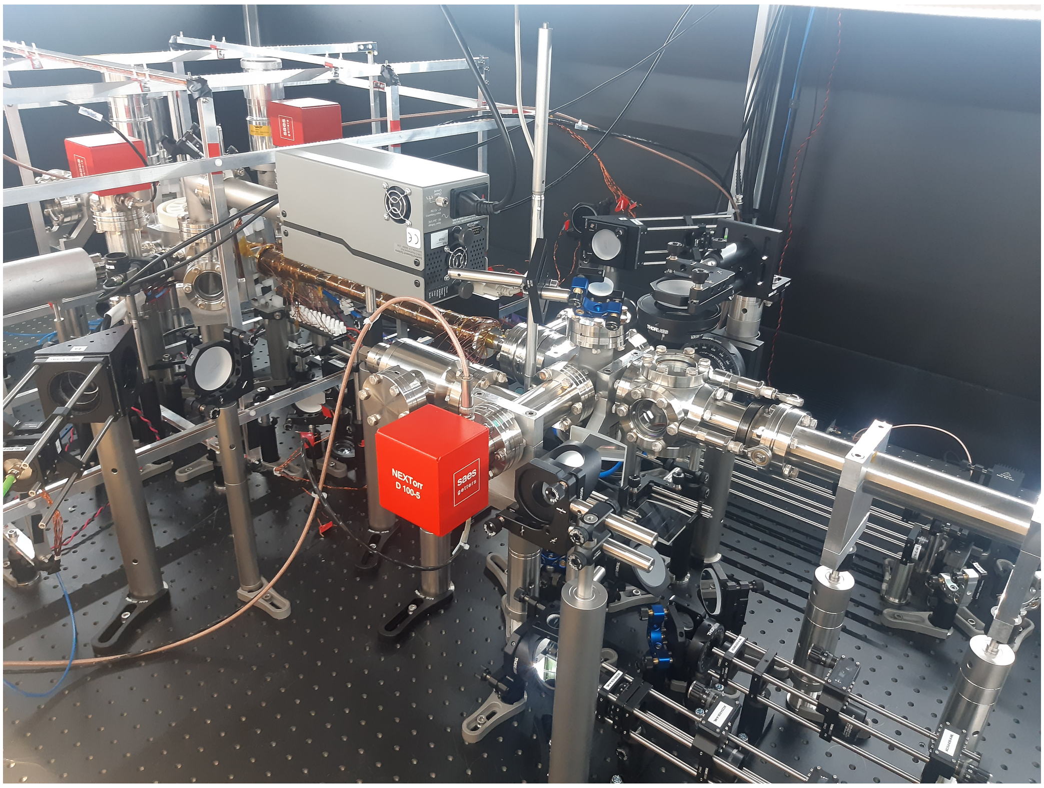

Figure 3: Photograph of the experiment. The oven and high-vacuum section is on the right and the ultra-high vacuum section, including the MOT chamber, are on the left.

2.3 Optical Trapping of a BEC in a Quasi 2D Uniform Potential

In order to cool the atomic cloud to quantum degeneracy, the atoms are captured in an optical dipole trap (ODT). Optical dipole traps confine atoms in the attractive potential of far red-detuned laser beams. The red detuning of the laser beam creates an attractive dipole potential for the atoms such that they are drawn to regions of high intensity.
This experiment makes use of a 45 Watts 1030 nm laser focused to a waist size of 35 µm. The atoms are transferred to the ODT from the cMOT. Currently, loading efficiencies of 10 % are reached. The focal point of the ODT beam overlaps with the MOT position in the center of the MOT chamber.
In the future, the atomic cloud will be moved to the science cell because optical access is possible from wider angles. This transport is enabled by using a pair of tunable lenses, that allow movement of the atomic cloud over 50 cm. Prior to the transport, the atoms will be pre-cooled to avoid atom spilling. Then the atomic cloud will be moved by slowly displacing the position of the ODT beam's focal point towards the science cell, where cooling to quantum degeneracy will be performed.
Finally, the BEC will be loaded into the quasi 2D pancake trap. The trap consists of an attractive 1030 nm sheet beam which provides confinement in the vertical direction combined with a repulsive potential of a blue-detuned box beam. The box beam is created by spatially modulating the intensity profile of a 371 nm laser using a spatial light modulator (SLM). The combination of the repulsive box potential and the attractive sheet beam

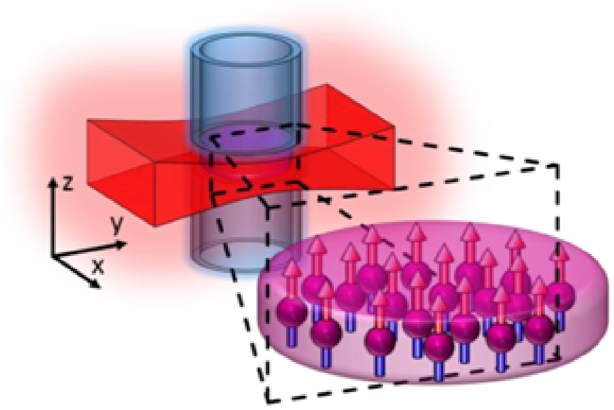

Figure 4: Sketch of 2D pancake trap. The red cuboid indicates the attractive sheet beam and the blue cylinder shows the repulsive box potential. In combination, a uniform quasi 2D pancake trap results (purple disk).

generates a uniform trapping potential, where we will perform the measurements suggested in Sec. 1.2. Fig. 4 depicts the described trapping configuration.

3 Requirements for performing Bragg Spectroscopy with a DMD

3.1 Optical Dipole Potentials

An external electrical field induces an electric dipole moment in an atom. The induced dipole moment is proportional to the polarisability of the atom and the electric field, $\mathbf{d} = \alpha \mathbf{E}_\mathrm{L}$. Here, α is the complex polarisability, which depends on the driving frequency ω_L. If the field frequency ω_L is far detuned from the atomic resonance ω_atom, the neutral atom will interact with the light field in a conservative manner. This means the atom will feel a conservative potential that can be used for trapping, cooling, or exciting the atom. The resultant dipole force can be written as [16]

$$\mathbf{F}_\mathrm{dip} = -\nabla \mathbf{U}_\mathrm{dip}, \tag{1}$$

where the potential is given by

$$U_\mathrm{dip} = -\frac{1}{2}\langle \mathbf{d} \cdot \mathbf{E} \rangle = -\frac{1}{2\epsilon_0 c}\mathrm{Re}(\alpha)\mathbf{I}. \tag{2}$$

For a field detuning Δ from resonance much bigger than both the Rabi frequency $\Omega = \frac{\mathbf{d} \cdot \mathbf{E}_\mathrm{L}}{\hbar}$ and the transition rate Γ, we find that

$$\mathbf{U}_{dip} = \frac{\hbar \Omega^2}{4\Delta} = \frac{\hbar \Gamma^2}{8\Delta}\frac{I}{I_\mathrm{sat}}, \tag{3}$$

where I_sat is the saturation intensity of the transition [39].
Eq. 3 shows us that any abritrary spatial potential can be created by modulating the light intensity. This is a useful tool for the field of ultracold atoms. We will implement this tool for the Bragg spectroscopy of dipolar quantum gases. The electric field intensity is modulated using a digital micromirror device (DMD). This chapter will give more information on the quantum optical background to Bragg excitation using a DMD and the optical limitations given by the imaging system.

3.2 Theoretical Background to Bragg Spectroscopy

In this section, we present the theorectical background of measuring the excitation spectrum of BECs using Bragg scattering. The momentum dispersion of a dipolar BEC is presented in Sec. 1.2. A dipolar quantum gas is excited by diffraction of a moving sinusoidal lattice potential. Excitation only takes place if the transferred energy and momentum to the condensate both match those given in the dispersion relation. After exciting the BEC with a Bragg pulse, a particular momentum state is populated if the excitation is close to resonance. The response to the Bragg pulse is given by the density of the population transfer from the ground state to the probed momentum state and can be measured using time-of-flight (TOF) spectroscopy. In this section, we will closely follow the work in [19] and [32].
Bragg scattering can be described as a two-photon **Raman process** involving paired stimulated absorption and emission. We use a two-level atom with two momentum ground

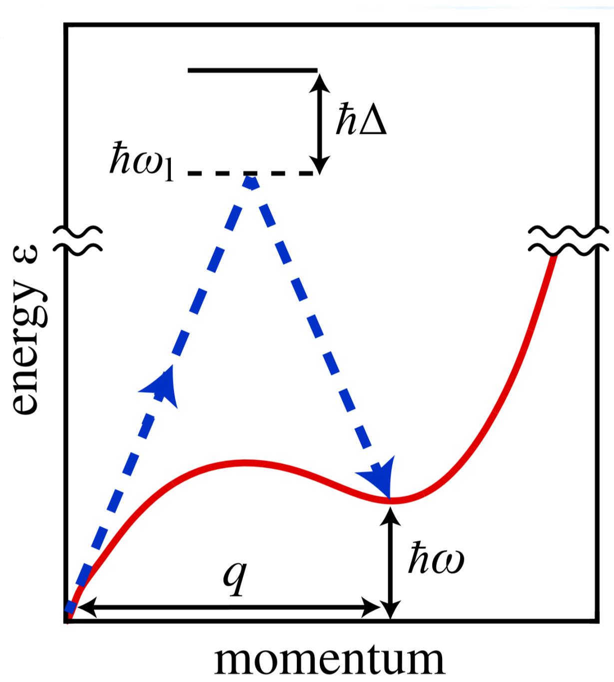

Figure 5: Stimulated Raman process of a Bragg scattering event in a dipolar quantum gas. An atom, initially at rest, absorbs a photon with energy ω_1 and reemitts a photon with energy ω_2 where the energy difference between the two photons is given by $\omega = \omega_1 - \omega_2 = E_{\text{Bragg}}/\hbar$. In this process the momentum q and the energy ω is transferred to the atom. The figure is taken from [33].

states, denoted as $|g, \mathbf{p_i}\rangle$, $|g, \mathbf{p_f}\rangle$ and $|e, \mathbf{p_i} + \hbar\mathbf{k_1}\rangle$ with the initial and final momentum states given by $\mathbf{p_i}$ and $\mathbf{p_f} = \mathbf{p_i} + \mathbf{q_r}$ as well as the momentum of the excited state $\mathbf{p_e} = \mathbf{p_i} + \hbar\mathbf{k_1}$. In the Raman picture, $|g, \mathbf{p_i}\rangle$ and $|g, \mathbf{p_f}\rangle$ are coupled to the excited state $|e, \mathbf{p_e}\rangle$ by two far-off resonant photons with frequencies ω_1 and ω_2. Momentum transfer into $|g, \mathbf{p_f}\rangle$ takes place through stimulated absorption of photons with frequency ω_1 and subsequent coherent stimulated emission of photons with frequency ω_2 via a virtual level detuned from $|e, \mathbf{p_e}\rangle$ by Δ, see Fig. 6. The atoms gain a recoil momentum in this process, which is given by $q_r = 2\hbar k \sin(\frac{\theta}{2})$ and depends on the magnitude of the wavevector of the laser beams $|\mathbf{k_1}| \approx |\mathbf{k_2}| = k$ and the angle of intersection θ of the two beams. The required excitation energy $E_{\text{Bragg}} = \varepsilon(p_i + q_r) - \varepsilon(p_i)$ is given by the dispersion relation of the atomic system. A succesful scattering event takes place if the detuning between the two photons matches the required energy transfer:

$$E_{\text{Bragg}} = \hbar(\omega_1 - \omega_2) = \varepsilon(p_i + q_r) - \varepsilon(p_i), \tag{4}$$

which in the case of the atoms being at rest initially reduces to $E_{\text{Bragg}} = E_r$, where E_r is the recoil energy. This gives a direct result for the recoil energy and thus enables us to measure the excitation spectrum. The process is displayed in Fig. 5.
By comparing a moving lattice potential with the interference pattern created by two laser beams with a detuning of $\Delta\omega$ intersecting at an angle θ we can find an alternative approach for describing the Bragg excitation.

The two laser beams are described by the following electric fields:

$$\mathbf{E}_j\,(\mathbf{r},\,t) = \boldsymbol{\epsilon}_j E_{0,j}\,\cos(\mathbf{k}_j\cdot\mathbf{r}-\omega_j t),\ j=1,2, \tag{5}$$

where $\mathbf{k}_j$ and ω_j are the wavevector and wavenumbers of the two fields, whereas $\boldsymbol{\epsilon}_j$ and $E_{0,j}$ are the unit polarisation vector and the amplitude of the fields. The interference pattern is given by the amplitude sum of the two electric fields $\mathbf{E}_{\mathrm{tot}} = \mathbf{E}_1\,(\mathbf{r},\,t) + \mathbf{E}_2\,(\mathbf{r},\,t)$ and leads to the total intensity

$$I\,(\mathbf{r},\,t) = \frac{\epsilon_0 c}{2}|\mathbf{E}_1\,(\mathbf{r},\,t)+\mathbf{E}_2\,(\mathbf{r},\,t)|^2. \tag{6}$$

Assuming equal amplitudes and polarisation for both fields and neglecting the fast oscillating term this can be rearranged to

$$I\,(\mathbf{r},\,t) = \epsilon_0 c E_0^2\cos\left(\frac{1}{2}(\Delta\mathbf{k}\cdot\mathbf{r}-\Delta\omega t)\right)^2, \tag{7}$$

with $\Delta\mathbf{k} = \mathbf{k}_1 - \mathbf{k}_2$ and $\Delta\omega = \omega_1 - \omega_2$.
Eq. 7 describes a moving lattice potential generated by the interference of two intersecting beams with a period $d = \frac{2\pi}{\Delta\mathbf{k}}$ and a velocity $v = \frac{\Delta\omega}{\Delta\mathbf{k}}$.
Moving back to the Raman picture allows us to find an expression for the Rabi frequency Ω_R of the transition $|g,\,\mathbf{p}\rangle \rightarrow\ |g,\,\mathbf{p{+}q}\rangle$. For a more detailed derivation please refer to [10] and [39]. We use a three-level Λ system as a starting point and reduce the system to an effective two-level atom, see Fig. 6.
The following wavefunction describes our three-level system:

$$|\Psi(t)\rangle = c_1(t)e^{-\frac{iE_{\mathbf{p}}t}{\hbar}}|g,\,\mathbf{p}\rangle + c_2(t)e^{-\frac{iE_{\mathbf{p+q}}t}{\hbar}}|g,\,\mathbf{p}+\mathbf{q}\rangle + c_{\mathrm{e}}(t)e^{-i(\omega_1+\Delta_1+\frac{E_{\mathbf{p_e}}}{\hbar})t}|e,\,\mathbf{p_e}\rangle. \tag{8}$$

The Hamiltonian of the three-level atom interacting with two light fields consists of two parts, the atomic part and the interaction part:

$$H_{\mathrm{A}} = \frac{\mathbf{p}^2}{2m}|g,\,\mathbf{p}\rangle\langle g,\,\mathbf{p}| + \frac{(\mathbf{p{+}q})^2}{2m}|g,\,\mathbf{p{+}q}\rangle\langle g,\,\mathbf{p{+}q}| + \big(\hbar(\omega_1+\Delta_1)+\frac{\mathbf{p_e}^2}{2m}\big)|e,\,\mathbf{p_e}\rangle\langle e\,\mathbf{p_e}|, \tag{9}$$

where the zero energy level is assigned to the state $|g,\mathbf{0}\rangle$. In the dipole and rotating wave approximation, H_{int} is written as:

$$H_{\mathrm{int}} = -\hat{\mathbf{d}}^+\cdot\mathbf{E}^- - \hat{\mathbf{d}}^-\cdot\mathbf{E}^+, \tag{10}$$

where $\hat{\mathbf{d}} = -e\hat{\mathbf{r}}$ is the electric dipole operator and $\mathbf{E}$ the total electric field as described above. Please note that in the following we set $|g,\,\mathbf{p}\rangle$, $|g,\,\mathbf{p}+\mathbf{q}\rangle$ and $|e,\,\mathbf{p_e}\rangle$ as $|g_1\rangle$, $|g_2\rangle$ and $|e\rangle$, respectively, and use the definition $\delta = \frac{\Delta_1-\Delta_2}{2}$ and $\Delta = \frac{\Delta_1+\Delta_2}{2}$. Using the expression for the Rabi frequency

$$\Omega_j := \frac{-\langle g_j|\boldsymbol{\epsilon}_j\cdot\mathbf{d}|e\rangle E_{0,j}}{\hbar},\ j=1,2 \tag{11}$$

we find for the interaction Hamiltonian

$$\begin{aligned} H_{int} =& \frac{\hbar\Omega_1}{2}\big(e^{-i(\mathbf{k_1}\cdot\mathbf{r}-\omega_1 t)}|g_1\rangle\langle e| + e^{+i(\mathbf{k_1}\cdot\mathbf{r}-\omega_1 t)}|e\rangle\langle g_1|\big)\\ &+\frac{\hbar\Omega_2}{2}\big(e^{-i(\mathbf{k_2}\cdot\mathbf{r}-\omega_2 t)}|g_2\rangle\langle e| + e^{+i(\mathbf{k_2}\cdot\mathbf{r}-\omega_2 t)}|e\rangle\langle g_2|\big).\end{aligned} \tag{12}$$

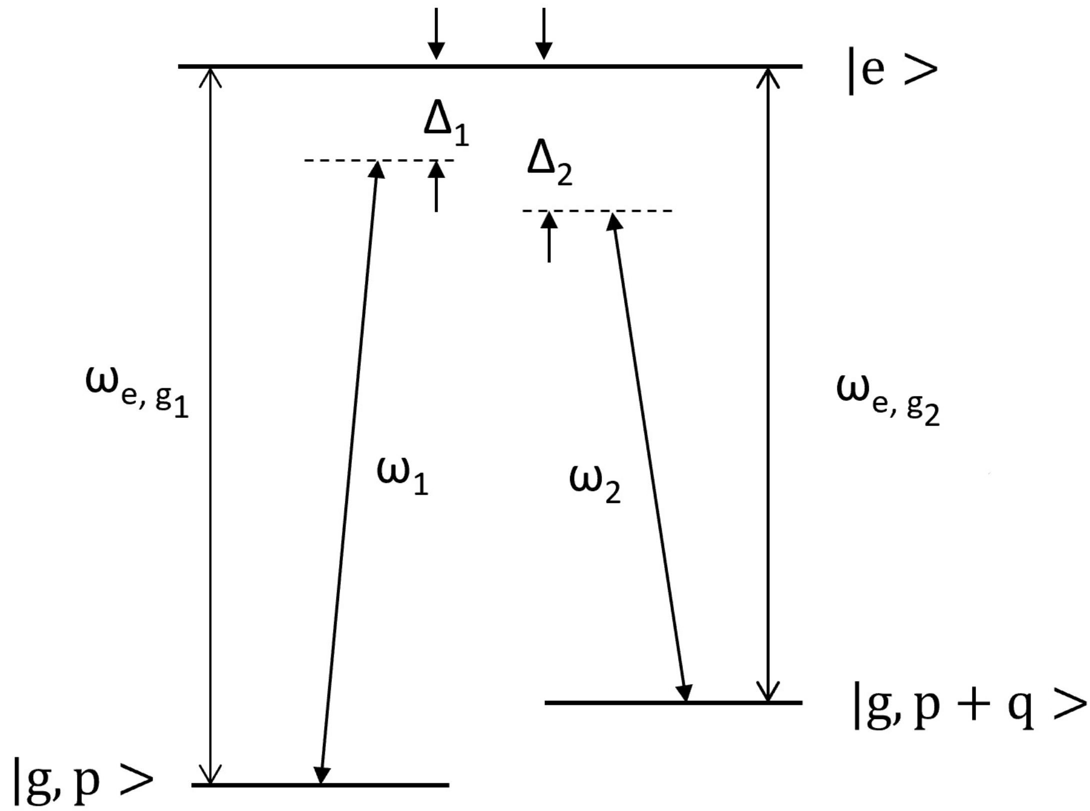

Figure 6: Three-level atom with excited state $|e\rangle$ and ground states $|g,\, \mathbf{p}\rangle$ and $|g,\, \mathbf{p}+\mathbf{q}\rangle$. The laser frequencies are detuned by $\Delta_{1,2}$ from the transition frequencies.

We use the unitary transformation to move into the rotating frame:

$$\begin{aligned}
\tilde{H}_{rot} =& \hat{U}\hat{H}\hat{U}^{\dagger} + i\hbar(\partial_t\hat{U})\hat{U}^{\dagger} \\
\tilde{\Psi}(t) =& \hat{U}\Psi(t) \\
\hat{U} =& e^{i(\frac{E_{\mathbf{p}}}{\hbar}+\delta)t}|g_1\rangle\langle g_1| + e^{i(\frac{E_{\mathbf{p}+\mathbf{q}}}{\hbar}-\delta)t}|g_2\rangle\langle g_2| + e^{i(\frac{E_{\mathbf{p}+\hbar\mathbf{k}_1}}{\hbar}+\omega_1+\delta)t}|e\rangle\langle e|.
\end{aligned} \tag{13}$$

After moving to the rotating frame, we find the following Hamiltonian :

$$\tilde{H}_{\mathrm{A}} = \hbar\big(\Delta|e\rangle\langle e| + \delta|g,\, \mathbf{p}+\mathbf{q}\rangle\langle g,\, \mathbf{p}+\mathbf{q}| - \delta|g,\, \mathbf{p}\rangle\langle g,\, \mathbf{p}|\big), \tag{14}$$

$$\tilde{H}_{\mathrm{int}} = \frac{\hbar\Omega_1}{2}\big(e^{-i\mathbf{k_1}\cdot\mathbf{r}}|g_1\rangle\langle e| + e^{+i\mathbf{k_1}\cdot\mathbf{r}}|e\rangle\langle g_1|\big) + \frac{\hbar\Omega_2}{2}\big(e^{-i\mathbf{k_2}\cdot\mathbf{r}}|g_2\rangle\langle e| + e^{+i\mathbf{k_2}\cdot\mathbf{r}}|e\rangle\langle g_2|\big). \tag{15}$$

The wavefunction can now be written as

$$\tilde{\Psi}(t) = c_1(t)e^{i\delta t}|g_1\rangle + c_2(t)e^{-i\delta t}|g_2\rangle + c_{\mathrm{e}}(t)e^{-i\Delta t}|e\rangle. \tag{16}$$

Using the time-dependent Schrödinger equation $i\hbar\partial_t\tilde{\Psi} = \tilde{H}\tilde{\Psi}$, we find the equation of motion:

$$i\hbar\frac{dc_1}{dt} = \frac{\hbar\Omega_1}{2}c_{\mathrm{e}}(t)e^{-i\Delta_1 t}\cdot e^{-i\mathbf{k_1}\cdot\mathbf{r}} \tag{17}$$

$$i\hbar\frac{dc_2}{dt} = \frac{\hbar\Omega_2}{2}c_{\mathrm{e}}(t)e^{-i\Delta_2 t}\cdot e^{-i\mathbf{k_2}\cdot\mathbf{r}} \tag{18}$$

$$i\hbar\frac{dc_{\mathrm{e}}}{dt} = \frac{\hbar\Omega_1}{2}c_1(t)e^{i\Delta_1 t}\cdot e^{i\mathbf{k_1}\cdot\mathbf{r}} + \frac{\hbar\Omega_2}{2}c_2(t)e^{i\Delta_2 t}\cdot e^{i\mathbf{k_2}\cdot\mathbf{r}}. \tag{19}$$

The equations of motions show a coupled set of differential equations which are difficult to solve. We will not develop the result in the three-level system because the excited state is damped to equilibrium instantaneously and not actually populated during the transition.
In the case of a Raman transition, the detuning from the excited state Δ is a lot bigger than the energy splitting between the two momentum ground states, the detuning from the resonant case ($\delta = 0$), and the individual Rabi frequencies:

$$|E_{\mathbf{p+q}} - E_{\mathbf{p}}| \ll \Delta,\ |\delta| \ll \Delta \text{ and } \Omega_{1,2} \ll \Delta.$$

Due to the large single photon detunings we can reduce the the three-level system to an equivalent two-level system using the adiabatic elimination method. The steps are carried out in [35] and do not add much to the understanding of the conducted work, which is why we do not discuss them in the scope of this thesis. The resulting two-level Hamiltonian is given by

$$\begin{aligned} H_{\mathrm{eff}} = &-\hbar\big((\delta + \frac{\Omega_1^2}{4\Delta})|g_1\rangle\langle g_1| + (-\delta + \frac{\Omega_2^2}{4\Delta})|g_2\rangle\langle g_2|\big) \\ &+ \frac{\Omega_{\mathrm{R}}}{2}(e^{i(\mathbf{k_2}-\mathbf{k_1})\cdot\mathbf{r}}|g_1\rangle\langle g_2| + e^{i(\mathbf{k_1}-\mathbf{k_2})\cdot\mathbf{r}}|g_2\rangle\langle g_1|), \end{aligned} \tag{20}$$

with

$$\Omega_{\mathrm{R}} = \frac{\Omega_1\Omega_2}{2\Delta}. \tag{21}$$

The populations of the states in the two-level system coincide with the populations of the two ground state, which are coupled with the effective Rabi frequency Ω_{R}. This result shows us that the effective Rabi frequency for a two-photon Raman transition $|g_1\rangle \longrightarrow |g_2\rangle$ is given by the depth of the moving lattice. Generating the moving lattice with two overlapping beams is equivalent to any other method.
From the form of H_{eff} and its non-diagonal terms it becomes obvious that the transitions $|g_1\rangle \longrightarrow |g_2\rangle$ and $|g_2\rangle \longrightarrow |g_1\rangle$ are accompanied by a momentum shift of $\mathbf{k_1} - \mathbf{k_2}$ and $\mathbf{k_2} - \mathbf{k_1}$, respectively.
Finally, we want to give an estimate of the laser intensities required to generate a Rabi frequency as high as $\Omega_{\mathrm{R}} = 2\pi\cdot 1$ kHz such that a full π-pulse has a duration shorter than 0.25 ms and we are not limited by lifetimes of the condensate. As mentioned in Sec. 2.2, the 583 nm transition is used for the Bragg spectroscopy where we introduce a detuning of $\Delta = 2\pi\cdot 360$ MHz from resonance. Eq. 3 shows the relation between the individual Rabi frequencies $\Omega_{1,2}$ and the laser intensity. This is related to the effective Rabi frequency Ω_{R} through Eq. 21. With the given absorption rate of $\Gamma = 2\pi\cdot 190$ kHz we obtain a required

laser intensity of $\frac{I}{I_{\text{sat}}} = 40$. The saturation intensity is given by $I_{\text{sat}} = 0.13\ \frac{\text{mW}}{\text{cm}^2}$, see [22]. To translate the laser intensity into power we assume an illumination area of the atomic cloud size with a radius of $r = 100\ \mu\text{m}$, so $P = I \cdot A = 1.6\ \mu\text{W}$. This estimate shows that very small laser powers are necessary to drive a full π-pulse in a duration of only 0.25 ms.

3.3 Bragg Potentials Created with a DMD

There are two ways to use a DMD to create the Bragg potential and induce a transition into a higher momentum state:

- Direct projection of a moving sinusoidal pattern.
- Holographic projection of a sinusoidal inteference pattern.

In both cases a single laser beam with a detuning Δ from resonance can be used to create the potential instead of using two laser beams with a detuning from one another. This has the advantage of not having to manually control a second frequency and the angle of intersection. A DMD can create binary patterns. When a laser beam is reflected from the DMD, this binary pattern is imprinted into the laser beam's intensity. Moreover, the DMD can create whole sequences of patterns and switch between them. This tool will be used to produce moving light potentials in the atom plane.

3.3.1 Direct Projection

With the direct projection method, the DMD creates a sinusoidal pattern and projects it onto the atomic plane directly. In this section, we will link the relevant parameters for this process with the resulting momentum and energy transfer. More detailed information on the experimental implementation can be found in [21].
As mentioned in Sec. 3.2, the resulting momentum and energy transfer depends on the wavelength of the pattern and the speed at which it moves. The sinusoidal pattern can be generated by the DMD directly. The lowest achievable wavelength will put an upper bound to our momentum range. This limit will be given by our minimum resolvable feature of our diffraction-limited imaging system:

$$\lambda_{\text{min}} = r_{\text{min}} = \frac{2\pi}{\Delta k_{\text{max}}}. \tag{22}$$

The sinusoidal pattern has to move across with a velocity v. It takes N steps to complete a movement of the pattern by one period. N needs to be sufficiently large to ensure a smooth pattern movement. The step size of each move is:

$$s = \frac{\lambda}{N}. \tag{23}$$

Assuming that the DMD changes frame with the refresh rate R, the speed of the pattern is given by:

$$v = R \cdot s = R \cdot \frac{\lambda}{N}. \tag{24}$$

This can be used to find an expression for the transition frequency:

$$\omega = \frac{v}{\Delta\mathbf{k}} = \frac{2\pi R\lambda}{N\lambda} = \frac{2\pi R}{N}. \tag{25}$$

The formula shows clearly that the maximum available transition frequency only depends on the maximum refresh rate and the number of steps used to create a movement of λ. Because N is fixed through the requirement to create a smooth movement, R determines the maximum frequency.

3.3.2 Holographic Projection

A holographic pattern is created in the atom plane by placing the DMD in the Fourier plane of the atoms. A sinusoidal pattern is the result of the Fourier transform of two delta functions, that are symmetrically positioned around zero. Extensive information on the experimental implementation can be found in [33] and [34].

Essentially, two delta functions convolved with a Gaussian envelope function are created with the DMD and will then be focused onto the atom plane. An additional grating structure is imprinted on the patches to set a phase relation between the two beams. The delta functions create an infinite sinusoidal pattern whereas the Gaussian envelopes lead to a spatial restriction of the pattern and can account for intensity dependent inhomogeneities. A Gaussian envelope is also required to ensure the reflection of a minimum amount of laser light. As a result, two degenerate light beams are focused onto the atomic plane where they interfere and create the sinusoidal pattern. In this case, the intersection angle of the two beams will determine the periodicity of the sine wave and thereby the resultant momentum transfer

$$\Delta k = 2k_{\mathrm{L}} \sin(\frac{\theta}{2}). \tag{26}$$

This formula shows that the maximum transferable momentum in a Bragg pulse depends on the wavelength of the laser light and the maximum achievable angle of intersection. Normally, the imaging setup sets an upper bound on the maximum angle of intersection with its numerical aperture. The angle can be varied by changing the distance of the two patches on the DMD screen.

Just interfering two degenerate beams would lead to a static sinusoidal pattern. However, it is possible to create an artificial frequency shift of one of the two beams. Here, we use the fact that the frequency is proportional to the time derivative of its phase

$$\Delta\omega = \frac{\partial\phi}{\partial t}, \tag{27}$$

such that employing a time dependent phase shift in one of the two patches relative to the other will lead to a frequency shift. This can be achieved by generating a sequence of changing patterns with the DMD. The phase is shifted by shifting the grating across the patch over a fraction of a period. A number of N frame changes are required to shift the grating by one period, such that a phase shift of

$$\delta\phi = \frac{2\pi}{N} \tag{28}$$

is created in one step. Considering frame changes with a repetition rate of R leads to a frequency offset of one of the beams relative to the other by

$$\omega = \frac{2\pi R}{N}. \tag{29}$$

This result is equivalent to the one worked out for the direct projection method (see Sec. 3.3.1).
As a result, both methods enable us to generate equal maximum Bragg transition frequencies and depend on the maximum switching rate of the DMD and the number of frames per period movement. The difference between the two methods lies in the maximum available Bragg momentum and depends on the imaging systems for both options. This will be studied in more detail in Sec. 4.1.
Finally, we want to investigate the parameters our imaging setup and switching rate need to perform to access the interesting region of the dispersion relation, where we take the results from [33] and [37] as a reference point.
The highest momentum state probed is given by $ql_z = 1.7$ whereas the roton minimum was found in the interval $ql_z = [1.27, 1.41]$. In the Innsbruck experiment, the harmonic oscillator length along the tight confinement is given as $l_z \approx 0.5$ µm, which translates to a maximum momentum $q_{\text{max}} = 3.4 \cdot 10^6$ μm^{-1} and requires a minimum pattern wavelength of $\lambda_{\text{min}} = 1.8$ µm.
The highest energy transferred is given by $\frac{\omega}{\omega_z} = 2$, with $\omega_z = 2\pi \cdot 256$ Hz. This results in an excitation energy of $\omega_{\text{max}} = 2\pi \cdot 512$ Hz. A value of $N = 9$ was used to obtain a smooth transition, which is the same value as used in [21]. This would require a maximum DMD refresh rate of R_{max}= 4.6 kHz.
These are first indications of where the relevant region in the dispersion relation lies. Nevertheless, the target is to generate a setup with the highest possible resolution and switching rate. Notice that Petter et al. use a different trap geometry (cigar-shaped) than our future experiment (pancake-shaped) which influences the excitation momenta and frequencies. Moreover, the excitation momentum and energy depend on the trapping frequencies which are subject to change according to experimental conditions.

3.4 Optical Limitations

In the last section, we derived that the maximum Bragg momentum depends on the resolution of the imaging system. This section gives more insight into the effects limiting the resolution of an imaging system, which are either of technical or fundamental origin. We will start with investigating the latter.

3.4.1 Diffraction-Limiting Angular Resolution

The minimum limit to the resolution of an optical system is given by its diffraction limit (see [18], [24] and [43]) which results from the nature of image formation.
Let's consider an object that is placed in the back focal plane of a collimating lense which is illuminated by a light beam. The object will imprint some transmission function into the light beam $f(x, y)$. The wave components of the object propagate towards the lens in the

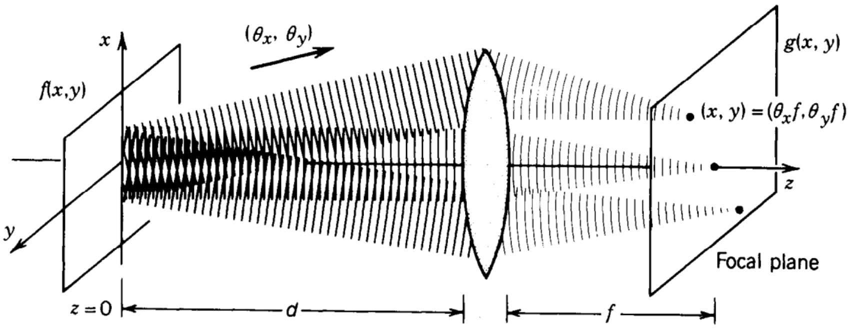

Figure 7: Fourier transformation in a lens. It is shown how different propagation angles in the object plane are transformed into spatial coordinates in the focal plane by a lens. The figure is adapted from [36].

form of rays in different directions . The lens will refract the rays and thereby translate the different angles into spatial positions. Therefore, it generates the spatial Fourier transform of the object transmission function in the beam profile, up to a phase curvature term. This term disappers in the Fourier plane of the lens, which is exactly at the focal point:

$$F(u, v) = \frac{1}{(2\pi)^2} \int_A f(x, y) e^{-i2\pi(ux+vy)} dA \tag{30}$$

where u and v are the spatial frequencies and A is the aperture area. Eq. 30 shows that an infinite aperture sized lens would generate the plain Fourier transform of the object whereas a limited aperture size filters out higher spatial frequencies. The spatial frequencies in the Fourier plane relate to the spatial coordinates (x', y') as follows:

$$u = \frac{x'}{f\lambda} \tag{31}$$

$$v = \frac{y'}{f\lambda} \tag{32}$$

with the focal length f.
Considering an object transmission function of $f(x, y) = 1$ with a circular aperture with diameter D leads to the following intensity distribution in the far-field (Fraunhofer) diffraction pattern:

$$I(\rho) = I_0 \Big[\frac{2J_1(2\pi\rho D/2)}{2\pi\rho D/2}\Big]^2 \tag{33}$$

where J_1 is the Bessel function of first order and ρ is the spherical spatial frequency. At a distance d' from the lens, the spatial frequency is given by:

$$\rho = \frac{\sin(\theta)}{\lambda} \approx \frac{r'}{d'\lambda} \tag{34}$$

with r' being the radial distance from the optical axis and θ the diffraction angle. The pattern that is created in the far-field through a circular aperture is called the *Airy disk*. In the focal plane, the first minimum is given at a radial distance from the optical axis by

$$r_{\text{Rayleigh}} = \frac{1.22\lambda f}{D} = \frac{1.22\lambda}{n\sin(\theta)}, \tag{35}$$

where θ is half of the largest angle that can be collected from the lens. This gives a definition for the numerical aperture of an optical element: $NA = n\sin(\theta)$. The first minimum from the optical axis is called the Rayleigh resolution. An object that creates two points in the image plane with a minimum distance r_{Rayleigh} can still be resolved.

3.4.2 Aberrations

There are additional factors that worsen the resolution of an imaging setup. We will consider effects that lead to distorted or blurred images called *aberrations*.
One distinguishes between two types of aberrations: chromatic and monochromatic. Since we are using only light of one laser, we can neglect the chromatic aberrations. The most relevant kinds of monochromatic aberrations are listed below:

- *Spherical aberrations*: These occur if lenses with spherical surfaces are present. Perfect shaped lenses have a non-spherical surface but are more difficult to produce. The small deviation to the perfect surface leads to aberrations where rays are not focused in one point. If rays are further from the optical axis, they will intersect the optical axis closer to the lens.
- *Comatic aberrations*: This is a kind of aberration that leads to changes in the magnification with respect to changing points in the image plane. Off-axis point sources appear to have a tail. It results from imperfections in the lens or imaging system.
- *Tilt*: A tilt occurs when the actual wavefront is tilted with respect to the optical elements or image plane. It results in an incorrect magnification throughout the image.
- *Distortion*: This effect leads to geometrical objects such as straight lines not appearing straight in the image plane but with a curvature. This results from a changing magnification or demagnification with increasing distance from the optical axis.
- *Defocus*: When the image plane is not in the focus of the imaging system, the image is not sharp but appears blurry.

Fig. 8 shows the traces of the rays if certain kinds of aberrations are present. Some of these aberrations can be prevented through a better alignment of the optical system whereas others can only be accounted for by either producing prefectly shaped lenses or using a combination of lenses where the aberrations cancel out.
The response of an optical system to a point source is called *point-spread function* (PSF) and determines the resolution of the system. If the aberrations are cancelled out and a diffraction-limited system is used, the first minimum of the PSF corresponds to the Rayleigh resolution. The image will be formed as a convolution of the amplitudes of the PSF and the actual pattern:

$$I_{\text{img}} \propto (A_{\text{PSF}} * A_{\text{pat}})^2. \tag{36}$$

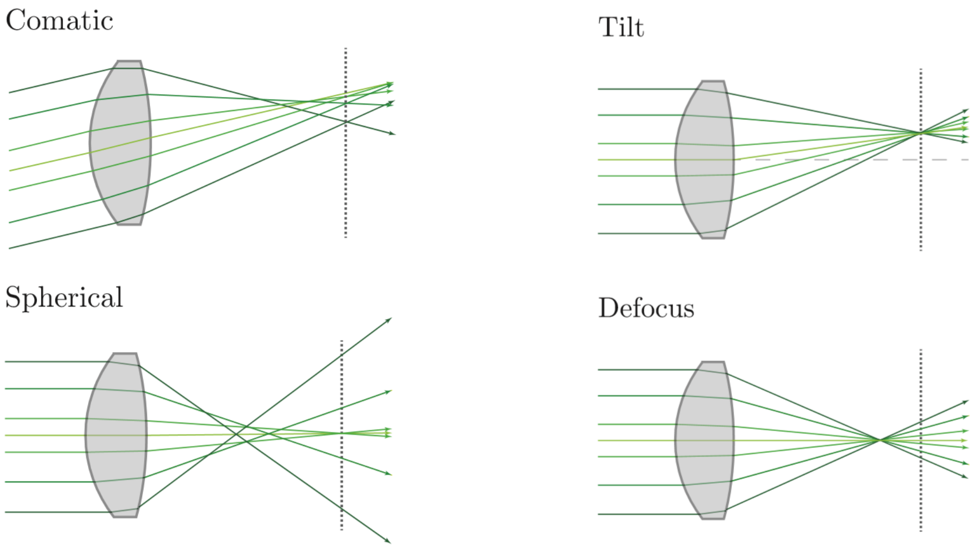

Figure 8: Different types of aberrations. The dashed line indicates the image plane. The figure is adapted from [43].

3.5 Digital Micromirror Device

The digital micromirror device is a tool for spatial light modulation [42]. A picture of it is shown in Fig. 9. The active chip is made of a pixelated screen with squared micromirrors. When the device is in use, each mirror can be addressed individually to be pointing to either the 'On' direction or the 'Off' direction, see Fig. 10 and Fig. 11. This is enabled by tilting the mirrors around the diagonal axis of the mirror by a tilt angle of $\pm 12°$ with respect to the surface normal. When the device is switched off, the mirrors are placed in the 'reset' position which is parallel to the surface normal. The device is controlled with a Matlab program via the computer.

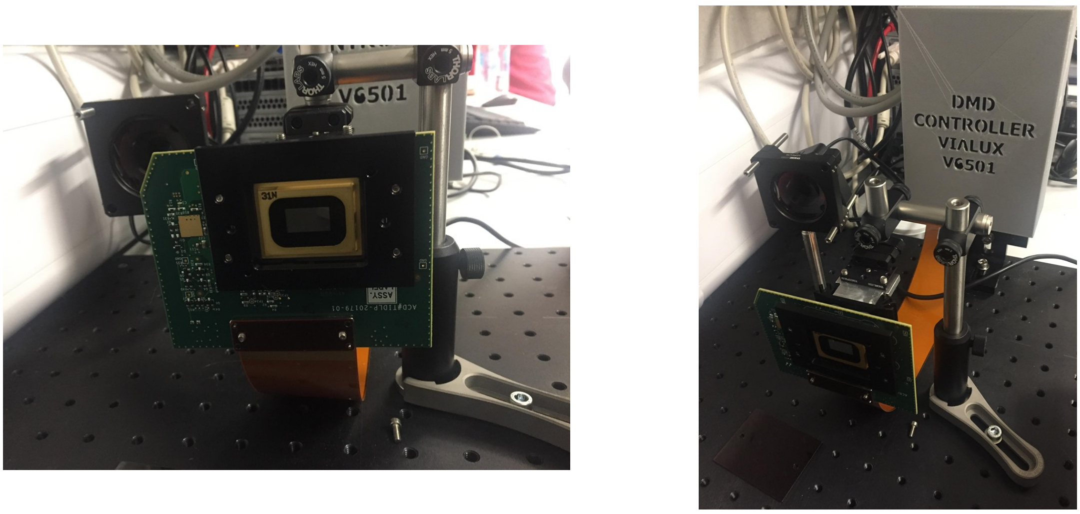

Figure 9: DMD model V 6501. We built a protection case for the electronics board and mounted the DMD on a home-built mount.

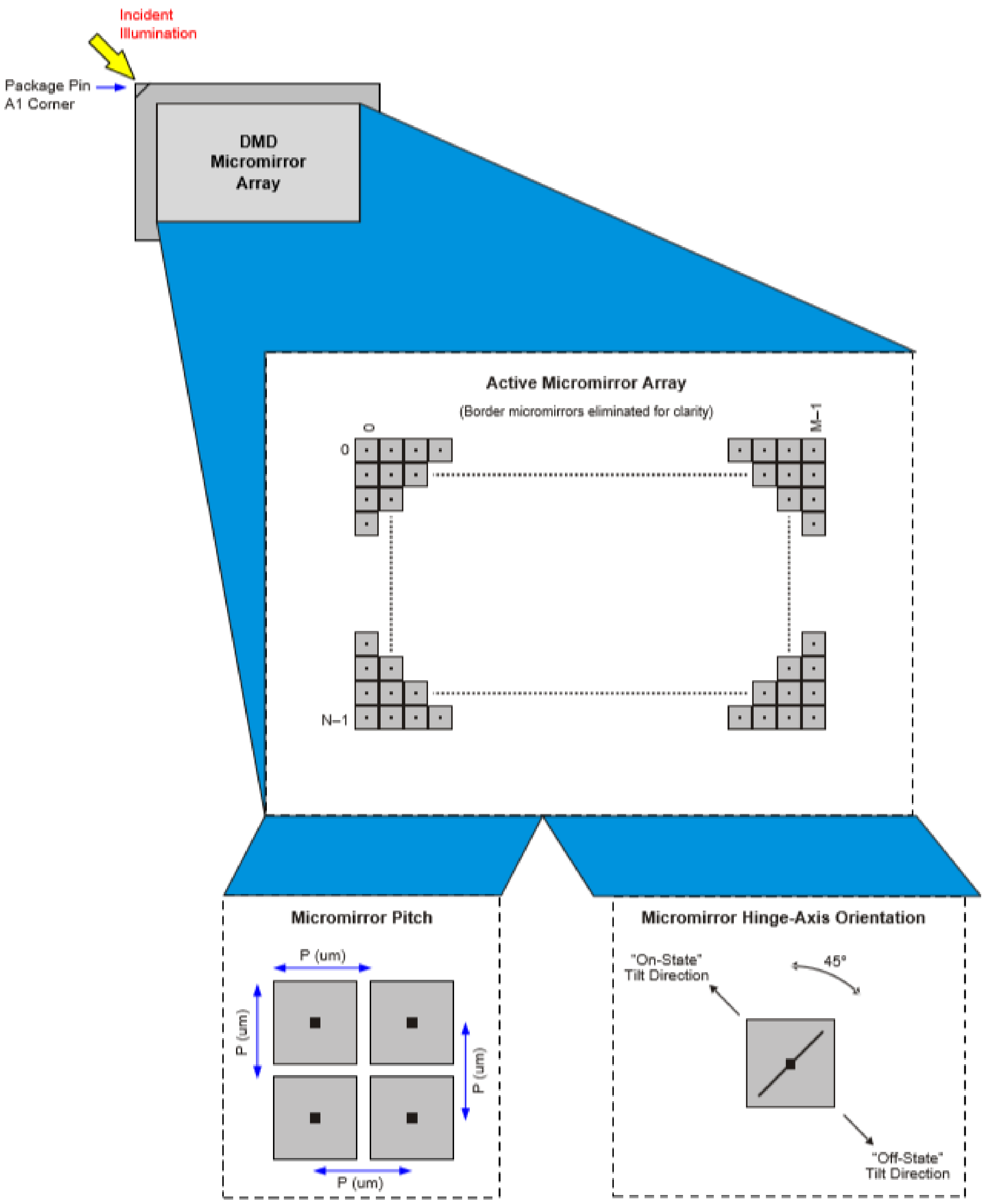

Figure 10: Active area of DMD. There are MxN micromirrors in the active array. Each one can be tilted along its diagonal axis to be pointing into the 'On' or 'Off' direction. The graphic is adapted from [42].

With this arrangement, the DMD acts like a grating where arbitrary patterns determine the structure of the grating. As a consequence of the grating-like structure, there are several orders of diffracted light, with a wavelength-dependent diffraction angle. We collect the 0^{th} order for the Bragg spectroscopy, by which we mean the diffraction angle which is closest to direct reflection and carries most of the reflected light intensity. Normally, the incident light is directed at such an angle that the brightest diffraction order in the 'On' direction is orthogonal to the surface of the DMD.

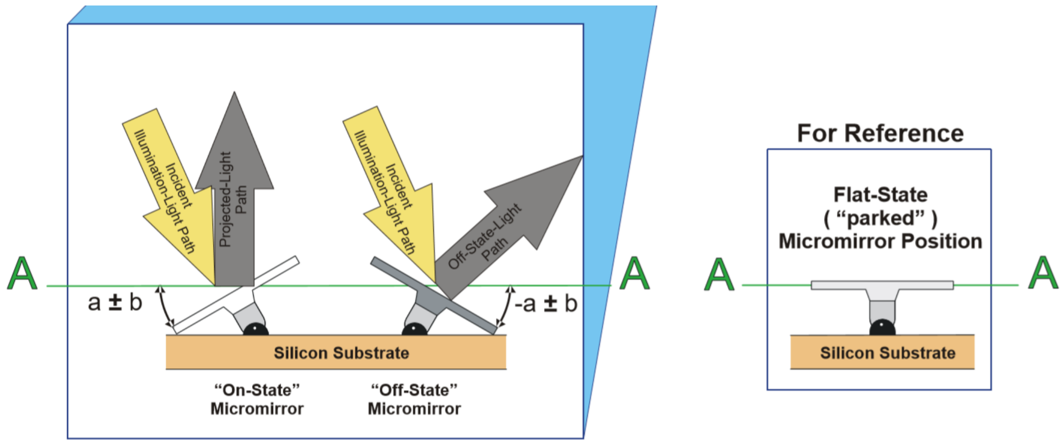

Figure 11: The beam path and its reflection off a DMD. The beam reflected into the 'Off' direction will be dumped. When the device is not in use, the mirrors are parked in a 'reset' state. The graphic is adapted from [42].

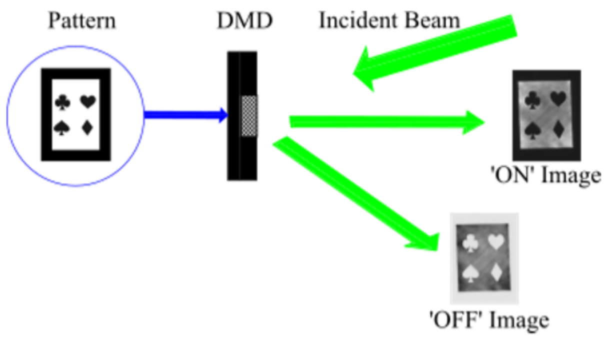

Figure 12: The projected pattern is displayed in the 'On' direction. A negative of the desired pattern is projected into the 'Off' direction. The figure is taken from [25].

The desired pattern is displayed with the DMD and is created in the 'On' direction. However, the negative of the pattern is automatically projected in the 'Off' direction, see Fig. 12.
In the experiment we use two different DMD models, V6501 and V7001. Originally, only the V6501 model was planned to be used but its delivery was delayed and we had the chance to start the experimental work with the V7001 model instead and compare the results obtained from both models. Both models use electronic hardware from Vialux that incorporates the DMD chip from Texas Instruments. Tab. 3 in Sec. A.1 offers an overview of the technical parameters of the two devices.
There are a few considerations which make one of the two devices more or less favourable for certain uses. We will examine these parameters throughout the following chapters to underline why we chose the V6501 model as the favourable DMD for the Bragg spectroscopy application.

4 Image Projection

This section describes the image projection of patterns generated by a DMD onto the atom plane. As mentioned in Sec. 3.3.2, the highest transferable momentum depends on the smallest achievable wavelength of the sine pattern and is limited by the resolution of our optical demagnification system. The experimental challenge is to design and build a demagnification system that has a sufficiently high demagnification and resolution to display the sine pattern.

4.1 Imaging System

As explained in Sec. 3.4, we rely on a high-resolution imaging system where we employ the direct projection method and use the V 6501 DMD model. The idea of the imaging system is to directly project a pattern displayed by the DMD onto the atom plane with an appropriate demagnification factor using a laser. The transition used for the Bragg spectroscopy is the 583 nm line such that a yellow laser is used in the setup.
The highest theoretically achievable momentum transfer in our experiment is given by the science cell geometry, which would allow a maximum incident angle of $\theta = 80°$. Using Eq. 35 we find a corresponding resolution of 1.1 µm. This value sets a lower limit to the resolution due to geometrical constraints but a more restrictive limit is given through the imaging system as described in Sec. 3.3.1. We want to find the demagnification factor required for our imaging system dependent on the minimum displayed wavelength.

4.1.1 Demagnification Factor

Using the estimate made in Sec. 3.3.2, we set a resolution target of $r_{\text{rayleigh}} = 1.5$ µm such that $\lambda_{\text{min}} = 1.5$ µm in order to access a slightly higher momentum than anticipated. Please note that when the lattice wavelength of the pattern becomes comparable to the resolution, the amplitude of the oscillation is reduced to a few percent, which can be balanced with the laser power.
We want to obtain an estimate for the minimum step size between adjacent sinusoidal frames $s_{\text{min}} = \frac{\lambda_{\text{min}}}{N}$. N needs to be big enough to generate a smooth transition between adjacent patterns. However, N can not be too large because a higher refresh rate is necessary to generate the same translation velocity which emphasises switching effects, see Sec. 6 for more details. We choose $N = 10$ and obtain an expression for the minimal step size between adjacent sinusoidal frames: $s = 150$ nm.
In order to find the demagnification factor that is required for our imaging system, we translate the minimum step size in the atom plane into a minimum step size in the DMD plane $s'_{\text{min}} = s_{\text{min}}M$, where M is the demagnification factor. The minimum step size in the DMD plane should be significantly bigger than a micromirror pitch such that a few pixels can be used to display a translation of a single step of the sinusoidal pattern in order to have sufficient level of greyscaling. We choose a minimum of two pixels per step size and get a required demagnification system with $M = 100$. The final image size in the atom plane, when using the whole DMD screen will be 145.9 µm x 82 µm, which is significantly bigger than the atomic cloud size.

This estimate shows that the V6501 model is more suitable because it has a smaller micromirror pitch than the V7001 model, which allows a higher level of greyscaling for the same demagnification system.

4.1.2 Objective

In order to achieve such a large demagnification factor a two stage arrangement is used, where the total demagnification factor is the product of the two individual factors. For the first stage a simple telescope consisting of two spherical lenses is used.
The second demagnification stage is more tricky to design because a larger demagnification factor in combination with a strongly focusing second lens is required. Moreover, the light has to pass a 2 mm thick glass cell before being projected onto the atoms. Building a second telescope using only two spherical lenses would involve significant aberrations and worsen the resolution of the system. Instead, the objective 'lens' consists of four lenses (see Fig. 13) which are chosen such that abberations cancel out. Additionally, the second telescope will have an aperture in the focus point of the first lens to employ spatial filtering.

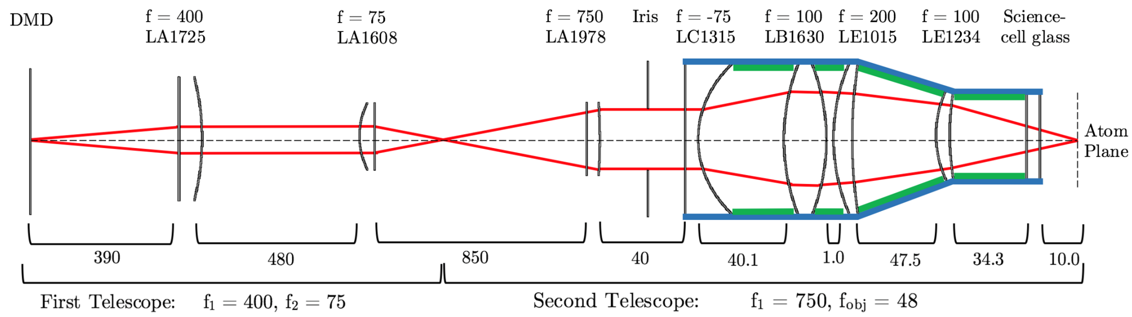

Figure 13: Imaging system consisting of two 'telescopes'. The first telescope uses long-focal length spherical singlet lenses, whereas the second telescope uses a custom objective as a replacement for the second lens. The lenses are labelled with their Thorlabs part numbers and focal length. The objective is displayed together with the final glass plate which is simulating the glass cell in the test setup. The distances are given in mm. The graphic was created by my co-worker Alexander Norden.

The objective has to fulfill a few requirements, given by geometrical constraints, such as maintaining a minimum distance from the glass cell and create a focal point exactly 1 cm behind the glass cell such that the focal point lies in the atomic cloud. This is done by finding a set of lenses, which in combination create the required focal length and resolution, and optimising their relative position using a home-built ray tracing program in Matlab. The objective is designed with inspiration from the custom-built objective presented in [4]. In the choice of the lenses we limit ourselves to easily obtainable commercial lenses with spherical surfaces. The resulting objective promises to create a resolution of 2.1 µm in the atom plane for a perfectly aligned setup. A total demagnification factor of 83 is reached. It was not possible to design an objective with a resolution of 1.5 µm, which would require more advanced lenses such as aspherical or achromatic lenses. However, the theoretical resolution of 2.1 µm and demagnification of 83 will be sufficient for a first design of an imaging system.
In order to test the imaging setup, we 3D printed a lens case and spacers with a precision

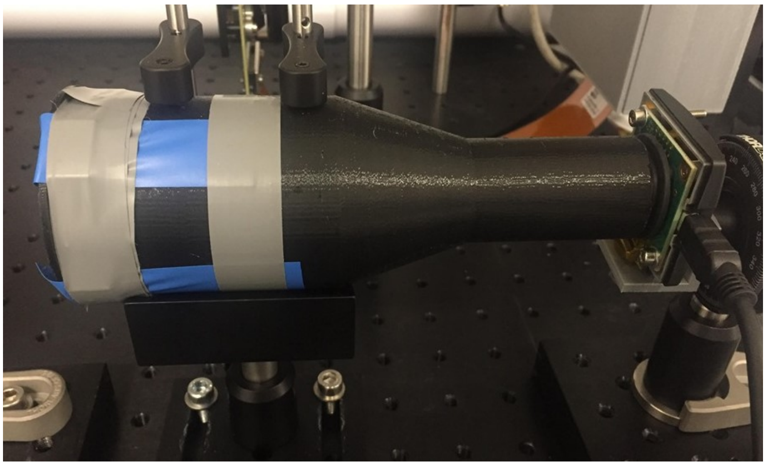

Figure 14: 3D printed objective case on a mount. There are additional holders at the left end of the objective that prevent the lenses from moving position and falling out of the objective. At the right end of the objective, a camera is installed right in the focal plane.

of 0.1 mm. The length of the spacers is calculated to fix the lenses at exactly specified distances. For simplification reasons, the glass plate (which simulates the science cell wall) is included in the objective for resolution tests. The ray tracing program also indicates which relative distances are the most sensitive in the whole setup. Whilst the setup is quite robust for lens movements in the mm range, a change of distances around 1 mm in the objective itself would worsen the resolution significantly. Fig. 14 shows the objective on a mount.

4.1.3 Imaging Setup

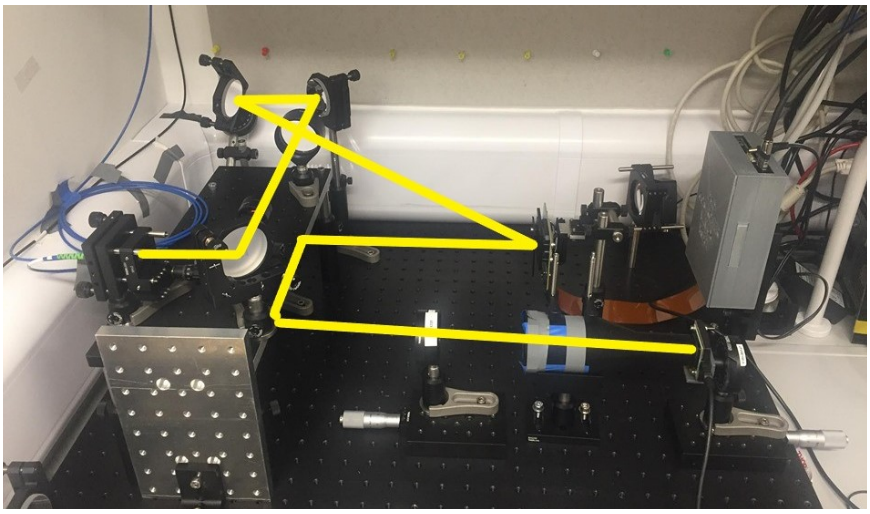

Figure 15: Test setup including laser beam path. The laser (shown in yellow) exits on the top left corner from an optical fibre and is directed to the DMD and through the second telescope. The displayed pattern is then captured with a camera that is placed in the atom plane.

The setup was built according to the plan shown in Fig. 13. For testing purposes, we only built the setup using the second telescope and neglected the first one. This is because the high demagnification factor would have resulted in a very small image, which is hard to display without an additional magnification stage. The additional magnification stage would again introduce aberrations and worsen the resolution. A DCC1545M Thorlabs camera is placed in the focal point of the objective (atom plane) to image the displayed pattern. Fig. 15 shows the whole setup with the final beam path.

4.2 Resolution Measurements

In this section we measure the resolution of our optical setup and compare it to the ray tracing predictions. As mentioned in Sec. 3.4, a final image is produced through the convolution of the point-spread function with the object itself [3]. The resolution tests are happening in one dimension where we test the sharpness of lines with known linewidths. These can be regarded as a set of rectangular functions in one dimension.
In 1D, the Airy disk forming the PSF can be approximated as a sinc function where the resolution corresponds to the width of the sinc function [1].
Since we are measuring our resolution using a camera with a finite pixel size, this will worsen the quality of the image and has to be taken into account in the analysis by convolving the image with a rectangular pixel function. The final image is then given by:

$$\begin{aligned} I_{\text{img}} &= (A_{\text{PSF}} * A_{\text{pat}})^2 * I_{\text{pix}} \\ &= \left(\text{rect}(\frac{x}{\text{boxwidth}}) * \text{sinc}(\frac{\pi x}{r})\right)^2 * \text{rect}(\frac{x}{\text{pixwidth}}) \quad (1\text{D}) \end{aligned} \tag{37}$$

4.2.1 Test Slide Measurement

The imaging system described in Sec. 4.1 has to be tested for its final resolution. This is done by producing an object and observing the corresponding image created by the imaging system with a camera. A laser beam is used to propagate the image through the imaging system.
Firstly, the resolution of the objective itself should be tested. A difficulty in testing the

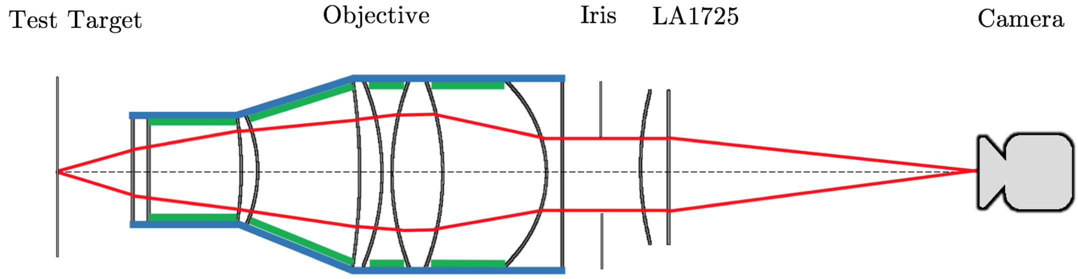

Figure 16: First setup for testing the objective's resolution. A test target is placed in the back-focal plane of the objective. The image is then focused onto a camera using a $f = 400$ mm lens. This setup has a magnification factor of 9. The graphic was created by my co-worker Alexander Norden.

resolution of the objective being part of a telescope as displayed in Fig. 13 is the finite pixel size of the DCC1545M Thorlabs camera (pixel width= 5.2 μm). If the resolution is tested this way, we need to be able to resolve features at the scale of 2.1 μm with the camera. The pixel size is clearly too big for this purpose, so we used a different approach to test the resolution.
The objective is flipped and used in combination with a $f = 400$ mm lens such that the resulting telescope acts as a magnifying system. We use a resolution test target from Thorlabs (NBS 1952), which consists of multiple sets of three lines each with known line widths. The lines on the test slide are shown as intensity dips because the transmission of the lines is zero. The test target is placed in the back focal plane of the objective. The 400 mm lens focuses the image onto the camera with an effective magnification factor of around 9 as shown in Fig. 16. This means, features in the order of the resolution are magnified to at least 18 μm in the image plane which corresponds to three camera pixels.
We use six sets of lines on the test slide with line widths ranging from 6.3 μm to 31.3 μm. The resolution can be determined by measuring the 'sharpness' of the edges of the lines and is obtained by fitting the cross section through the lines with Eq. 37. The fitting parameters are the width of the sinc function and the boxwidth of the rectangular function. We keep the pixel width constant. The result for the boxwidth gives us the magnification factor $M = \frac{\text{Boxwidth}}{\text{Linewidth}}$. We determine the resolution of the imaging system by dividing the sinc width through the magnification factor.

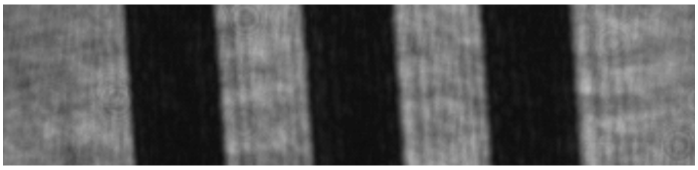

Figure 17: The figure shows a section of the camera measurement using the set of three lines with a linewidth of 25 μm. The camera is tilted by 4° relative to the test target.

Even though we flipped the telescope and only need to resolve features in the order of three camera pixels, we use a trick to improve our sampling even more. The camera is mounted on a rotation mount and is tilted by a certain angle before taking the pictures. An example camera shot is shown in Fig. 17. By adding multiple cross section rows together with a shifted origin we have more data points per camera pixel. The rows are shifted by the tangens of the tilting angle. The angle is chosen to be around 4° which increases the sampling rate by a factor of 10. In total, twenty rows are added together. Finally, we can account for background noise and dust particles by taking a background picture where the test slide is removed from the setup and dividing the original image by the background image.
The results of the measurements are summarised in Tab. 1. The data is fitted to a curve according to Eq. 37, where the error is given by the statistical uncertainty of the fit. Two example fits to the cross sections are shown in Fig. 18.
The resolution varies from measurement to measurement between 1.94 μm to 2.45 μm with a weighted average and standard deviation of $r = 2.18 \pm 0.19$ μm. This variation might occur because the lines are positioned on different areas on the test target. The objective

Linewidth (µm)	Magnification	Resolution (µm)	Boxwidth (camera pixels)
31.3	10.3	2.36 ± 0.01	62.2
25	9.0	2.45 ± 0.02	43.4
17.9	9.0	2.19 ± 0.03	30.9
12.5	9.1	2.37 ± 0.02	21.7
8.9	9.0	2.15 ± 0.08	15.4
6.3	9.0	1.94 ± 0.04	10.9

Table 1: Fitting results of the objective's resolution measurement for six different sets of lines.

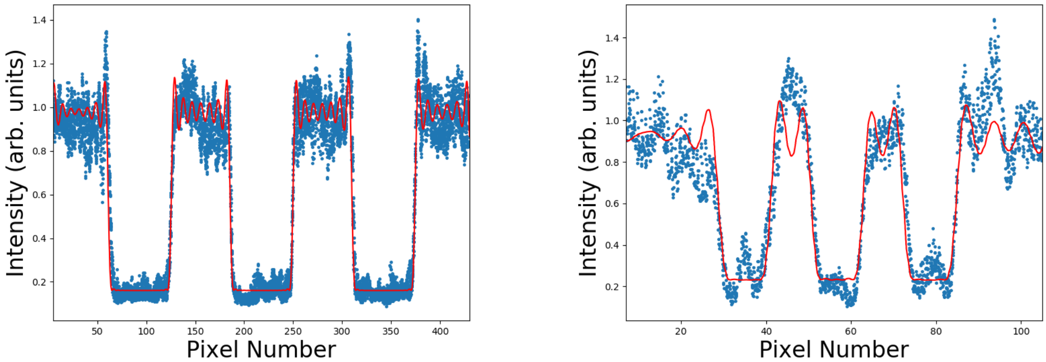

Figure 18: Cross sections through the test slide lines. For both measurements, twenty rows are added together. The fitting function is shown as a red curve. The linewidths of the curve are 31.3 µm for the left graph and 6.3 µm for the right graph. The resulting resolutions are given by 2.36 µm for the left graph and 1.94 µm for the right graph. Please note, that the lines are indicated by dips in the intensity because the test slide is not transmitting light at the line's position.

only guarantees the resolution of 2.1 µm for objects which are within 20 µm radius to the optical axis. Off-axis effects reduce the resolution. However, the lowest value of 1.94 µm and the weighted average of 2.18 µm confirm that the resolution of the objective is very close to the ray tracing predictions. The graphs and corresponding fits of the other lines are found in Sec. A.4.1.

4.2.2 DMD Resolution Measurement

In addition to measuring the objective's resolution as described in the last section, we want to measure the resolution of the imaging system itself. This is done by using the DMD in combination with the camera and the second telescope, consisting of a 750 mm lens and the objective, as shown in Fig. 19. We do not add the first telescope in this measurement yet, because the resulting image will be too small to be observed in the atom plane with a camera. Moreover, the first telescope is not limiting the system's resolution and therefore is not a critical part in the measurement. The DMD model V6501 is used for the resolution measurements.
As mentioned in the last section, we now have to measure the resolution with our camera setup directly and cannot make use of a magnification telescope as previously done. This

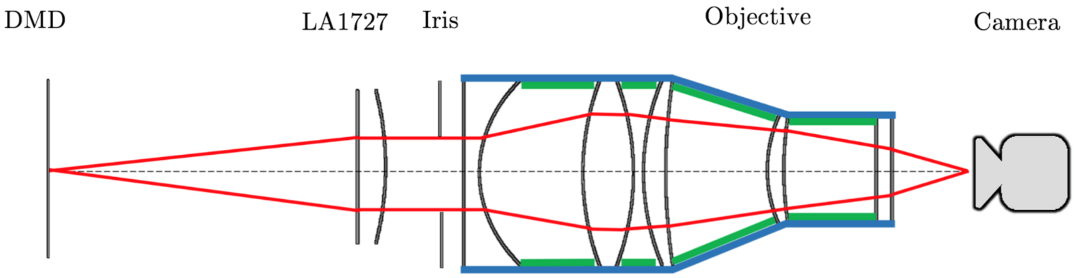

Figure 19: Test setup for the resolution measurement of the imaging system. The DMD produces a pattern that is imaged onto the camera with the 750 mm lens and the objective. The total demagnification factor of the setup is 15. The graphic was created by my co-worker Alexander Norden.

problem can be partly overcome by mounting the camera on a x-y translation stage. We use a rotation mount in combination with the translation stage to enable a movement of the camera in the micrometer range. The setup of the translation stage is shown in Fig. 20.
By moving the camera in small steps, we can take a lot of pictures and overlap them with a shifted x-axis position. This method is similar to what we have done for the previous measurement. Here, we overlap a series of twenty pictures per measurement. The shift of the x-axis accounts for the movement of the camera. Since the camera moves by steps which are only a fraction of the pixelsize, each pixel will measure a different intensity after a movement of a single step and thus enables us to recreate the actual image with a sub pixel-size resolution.
The pattern used to determine the resolution of the system is a series of six lines made of 50 DMD pixels each. This translates to line widths in the atom plane of 25.3 µm. A single shot of the pattern is shown in Fig. 21. The figure also indicates the regions on the image that are used for fitting in order to obtain the resolution dependent on the position of the camera.
The resulting data is fitted to Eq. 37. Here, the boxwidth and the pixelwidth are fixed and

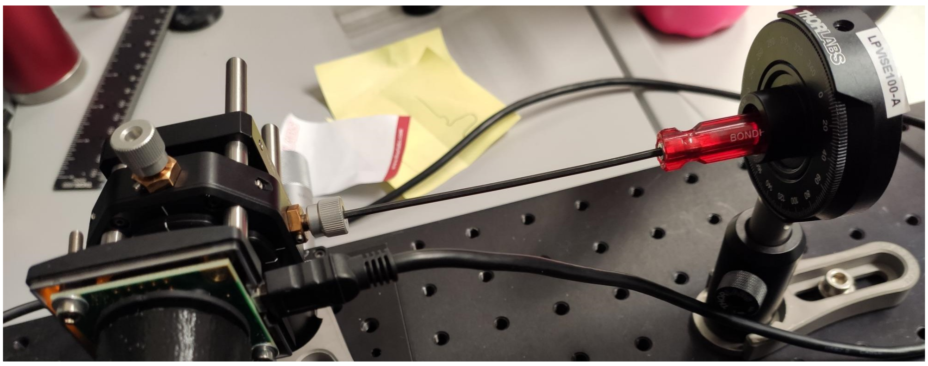

Figure 20: Translation stage setup for moving the camera in the x-y plane. The translation stage moves the camera a certain amount per turn. By connecting the translation stage with the rotation mount, we can accurately move the camera in micrometer steps. Please note that the movement is only possible in the x-direction with this setup.

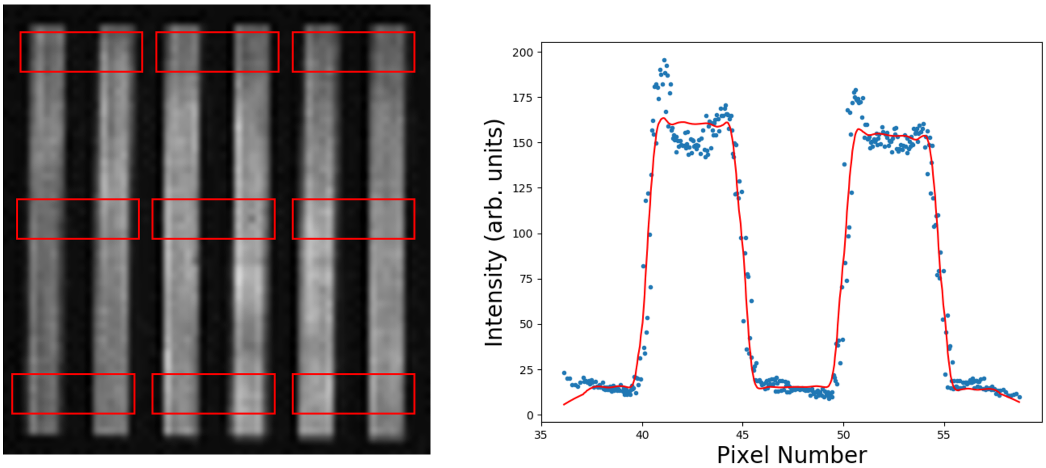

Figure 21: The left part of the figure shows a single shot of the line pattern created by the DMD. A set of 6 lines are used. The pattern will move across the x-direction of the camera such that more pictures are overlapped to find the actual system resolution. The red areas indicate 9 different regions on the image that we use to fit the data and find the imaging resolution. A combination of two lines is used for each fit. The data of the center region and the resulting fit is shown on the right.

the resolution results from the width of the sinc function. We combine a set of two lines for each fit such that we have nine different regions that are used for the fitting, see Fig. 21. An example fit of the center region of the image is shown in Fig. 21. The remaining fits are shown in Sec. A.4.2.

Region	Resolution (µm)
ML	2.58 ± 0.02
MM	2.59 ± 0.02
MR	2.32 ± 0.02
UL	2.34 ± 0.02
UM	2.61 ± 0.02
UR	2.54 ± 0.04
BL	2.57 ± 0.02
BM	2.49 ± 0.07
BR	2.69 ± 0.08

Table 2: Fitting results of the imaging system's resolution measurement. The abbreviations indicate the position on the camera, where for example upper left is indicated by 'UL'.

Tab. 2 summarises the results of the analysis, where the error is given by the statistical uncertainty of the fit. The results suggest that the resolution is quite homogenous along the image area, which is given by 300 µm x 300 µm. The weighted average and standard deviation is given by $r = 2.55 \pm 0.12$ µm. This resolution is not as low as the 2.18 µm we obtained in the objective's resolution measurement but gives an upper limit to what the actual resolution of the imaging system is. Although we are using the moving camera method, it might still be difficult to obtain reliable measurements of resolutions which are as small as 2 μm due to uncertainties in the camera movement. However, some of the measurements show a lower resolution value, which is promising for the future experiment. By doing a more careful alignment and choosing a proper magnification system that is used for magnifiying the image formed in the atom plane, we might get a better idea of the lower limit to our resolution of the whole imaging system.

To summarise, we tested the resolution of the objective and the imaging system with two different tests. The measurement of the objective's resolution delivers a lower bound for the total imaging system's resolution of 2.18 ± 0.19 μm. We found an upper bound for the resolution of the imaging system of 2.55 ± 0.12 μm. A next step would be to measure sine patterns directly with the target minimum wavelength. For this purpose, a good magnification system has to be designed and built so that the camera sees a magnified image of the atom plane image. The challenge is to achieve a small enough resolution for the magnification system such that our measurement is not falsified by the magnification system.

5 Pattern Formation and Correction

By using a DMD to create arbitrary light potentials we are limited to a binary image. Greyscaling will help us in creating non-binary patterns in the image plane. Moreover, the projected pattern has to be homogenous over the size of the atomic cloud and resemble the sinusoidal intensity profile accurately. A pattern correction algorithm accounts for aberrations and the Gaussian beam profile of the laser beam projecting the sine pattern.

5.1 Greyscaling and Image Binarisation

Due to its binary nature, the DMD does not intrinsically have greyscale ability. It can only display binary patterns. Greyscaling can be achieved through temporal or spatial averaging. For the purpose of cold atom experiments, spatial averaging is the favourable method because temporal averaging might induce additional effects with the atoms.
For effective spatial averaging, a minimum number of pixels are required to form a point in the image plane. Using our target resolution as the minimum point size we can estimate the number of pixels used for projection onto that same point. There are approximately 20x20 pixels that are projected onto a point of the resolution size in the image plane. This is sufficient for efficient greyscaling.
The binarisation of images with a pixel depth bigger than one can be done by using a dithering algorithm. The most famous one is the Floyd-Steinberg error diffusion algorithm [15]. It is developed in such a way that an image which is completely grey (50 % for all pixels) will be transformed to a black and white checkerboard. There are a few principles which describe how the algorithm works:

- The binarisation happens pixelwise. It starts with the top left pixel and works its way from left to right and top to the bottom of the image.
- The pixel to be binarised is rounded to be black or white (0 or 1). Then the error from the target value is calculated and passed on to the pixels on the right and the bottom of the pixel under examination. The error is weighted with a factor before passing it on to the next pixels, see Fig. 22, where the factors are calculated to produce a black and white checkerboard for a completely grey input image.

The binarised image is calculated with the algorithm given in Sec. A.2. Fig. 22 shows the binarisation process for pixel (i,j). Pixels on the left and top of the current pixel have already been binarised. The current pixel is rounded to 0 or 1 and the rounding error is passed on and added to four adjacent pixels, on the right, bottom right, bottom and bottom left of the current pixel.

5.2 Pattern Correction

There are additional factors that worsen the quality of an image. These arise from diffraction and aberration effects, the inhomogeneous laser intensity throughout its cross section and misalignment effects. It is possible to compensate for these effects with an iterative pattern correction algorithm, which we developed. For example, an inhomogeneous laser intensity

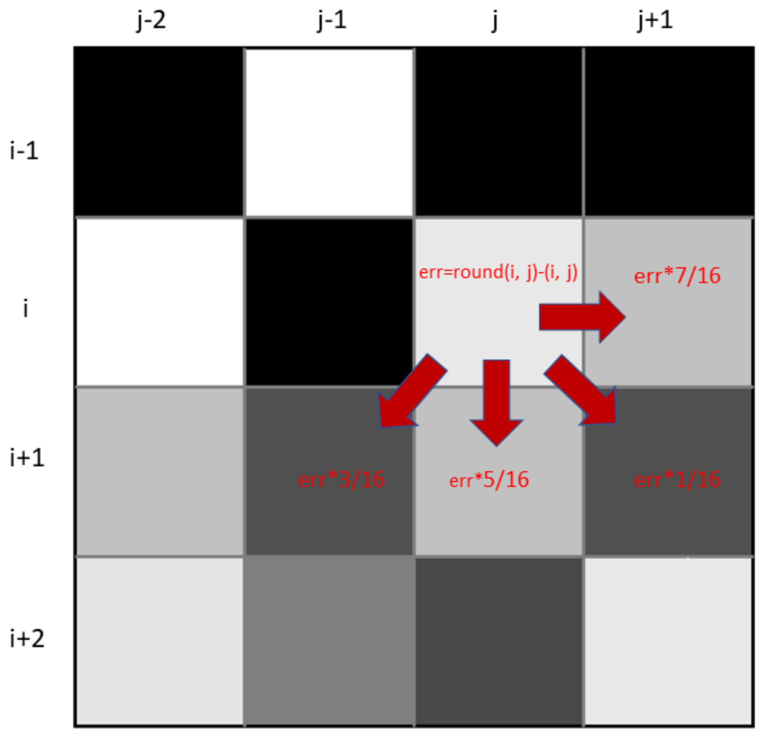

Figure 22: The Floyd-Steinberg binarisation process for pixel (i, j).

can be compensated by turning off more mirrors in the center of the DMD screen in order to match the overall intensity level to that of the side regions.
The pattern correction happens in an iterative sequence, which is displayed in Sec. A.3. The target pattern is called I_{targ}. It is binarised to give I_{bin} and sent to the device. A camera is placed in the atom plane and measures the resulting image I_{meas}. The measured picture has to be resized to match the DMD image size.
It is then compared to an intensity-corrected target picture I_{corr} to find an error function. The target picture needs to be intensity corrected because it is not possible to raise the intensity level on the side region but only to lower the intensity level of the central region. The maximum intensity is varied for different measurements whereas an additional offset of 10 bytes is added to I_{corr} during each iteration to account for background noise.
The error is calculated using a hyperbolic tangent function to treat large errors more gradually. The measured image is level-corrected to the level of the intensity-corrected target image. An additional factor of 5 in the hyperbolic tangent adds an extra stretch factor for the error and was experimentally optimised to avoid large errors preponderating.
Finally, the new picture is calculated by adding the error value to the original target picture I_{targ} and binarising it. The calculated picture is then sent to the DMD to snapshot a new measured picture and repeat the iteration step. The following equations describe the first

step of the iteration process:

$$\begin{aligned}
\mathrm{I_{err}} &= 255 \cdot \tanh\left[\frac{5}{255}\left(\mathrm{I_{meas}}\frac{\mathrm{sum(I_{corr})}}{\mathrm{sum(I_{meas})}} - \mathrm{I_{corr}}\right)\right] \\
\mathrm{I_{new}} &= \mathrm{I_{targ}} - m \cdot \mathrm{I_{err}} \\
\mathrm{I_{bin}} &= \mathrm{Floyd_Steinberg(I_{new})}
\end{aligned} \tag{38}$$

5.3 Pattern Correction and Greyscaling Measurements

The pattern correction algorithm was tested using the setup as described in Sec. 4.1. For the imaging setup, only the second telescope was in use to avoid the magnification factor being too high to image the displayed pattern. A set of sine patterns with six different wavelengths was used. The wavelengths range from 150 DMD pixels to 30 DMD pixels, which translates to wavelengths in the atom plane of 76 µm to 15.2 µm. Moreover, the pattern is optimised using three different target intensities $\mathrm{I_{corr}}$. For these measurements, an error weighting factor of $m = 0.1$ was used. An example of an optimisation procedure is shown in Fig. 23.

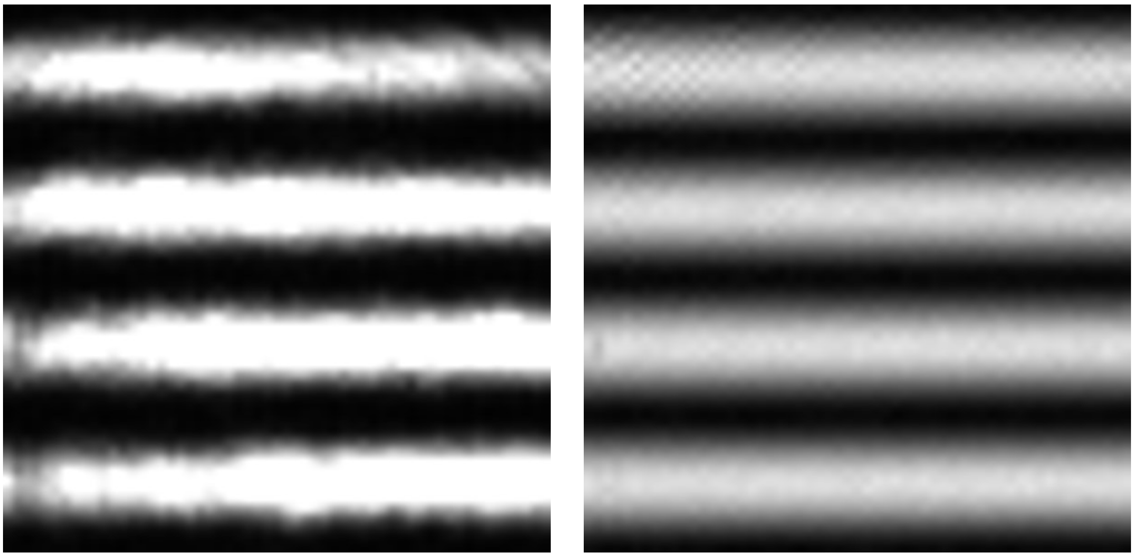

Figure 23: Sinusoidal pattern with a wavelength of 150 DMD pixels before (left) and after (right) application of the pattern correction algorithm. To reach this optimised pattern, eleven iteration steps were used. In the left picture, a clearly inhomogenous maximum intensity over the image area is visible, which partly saturates the camera. The target intensity was set to be 82% of the maximum intensity.

In order to find an estimate on how well the optimised pattern is portraying the target pattern, a crosssection of the pattern (corresponding to one column) is fitted to the following function:

$$f(x) = \sin\left(\frac{\pi}{\lambda}(x - x_{\mathrm{offset}})\right)^2 \cdot (y_{\mathrm{max}} - y_{\mathrm{offset}}) + y_{\mathrm{offset}}. \tag{39}$$

Fig. 24 shows the fitting results for two different wavelengths. The iterations were performed for a set of six different wavelengths and three different target intensity levels. The shorter wavelengths show a higher deviation from the sinusoidal pattern.

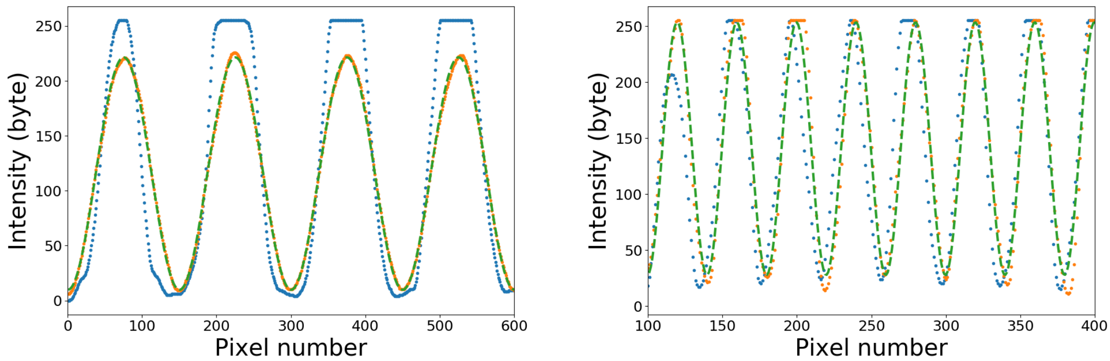

Figure 24: Cross sections of two sinusoidal patterns before and after optimisation with the corresponding fit to the optimised pattern. The target intensity was set to be 82 % of the maximum intensity. The starting pattern is indicated with blue dots, the optimised pattern is shown with orange dots and the fit is displayed by a green dashed line. The left figure uses a wavelength of 150 DMD pixels whereas the right figure uses a wavelength of 40 DMD pixels. As is clearly visible, the constant offset is a lot higher for the smaller wavelength and also the target intensity value (210) is not reached.

5.3.1 Mean Squared Error Progression

We start by analysing how well the pattern manages to resemble that of a sinusoidal curve. For this purpose, we fit the dataset of each iteration step to the function displayed in Eq. 39 and calculate the mean squared error. Fig. 25 shows the development of the mean squared error for all six wavelengths and all three target intensity levels.

Fig. 25 shows that the mean squared error is decreasing with increasing iteration number. This means that the pattern correction is improving the image quality and leads to more homogeneous sinusoidal patterns. It is independent on which target intensity is used during the iteration process. However, for the small wavelengths the lower target intensity value produces smaller errors. Another feature is that the overall error and the smallest error reached in the iteration process is a lot lower for higher wavelengths (err_{min} = 3.7 bytes^2 for λ = 150 pixels against err_{min} = 601 bytes^2 for λ = 30 pixels).

5.3.2 Final Intensity vs. Target Intensity

Moreover, we analyse how the final intensity maximum and offset evolve with the wavelength and if they depend on what is set as a target intensity.

For each iterative measurement, the cross section of the optimised picture is fitted to the function given by Eq. 39 and the intensity maximum and offset are extracted. As mentioned in Sec. 5.2, the target pattern uses a varying maximum intensity target value and a constant offset of 10 bytes. Fig. 26 shows what actual intensity value is reached dependent on the wavelength and the maximum target intensity.

Fig. 26 shows the maximum and offset intensity reached after optimisation. Both values decrease for increasing wavelength and get closer to the target value. The offset is independent on the maximum target intensity whereas the maximum intensity depends on the

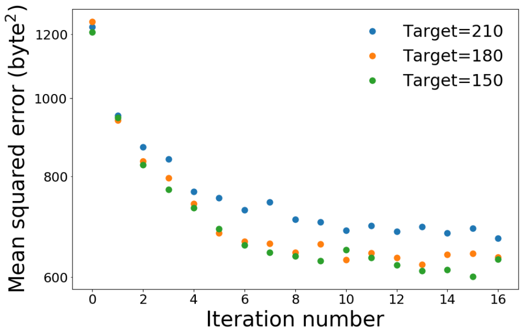

(a) λ= 30 pixels

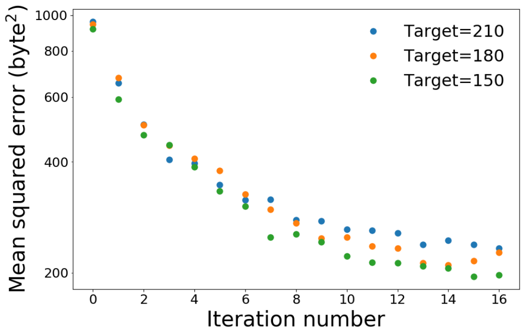

(b) λ= 40 pixels

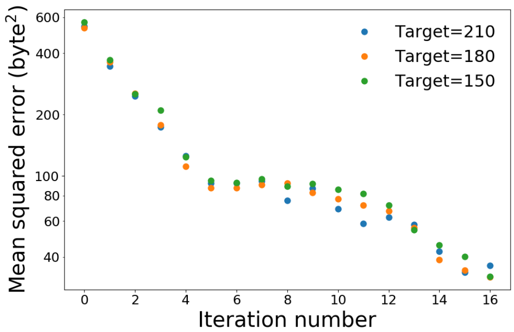

(c) λ= 60 pixels

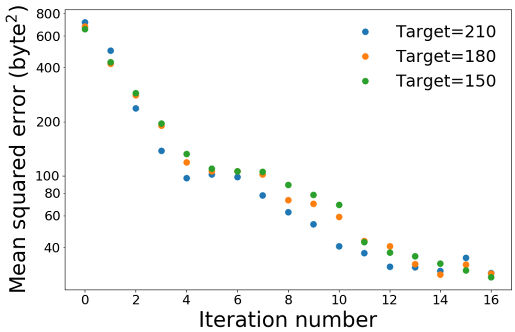

(d) λ= 80 pixels

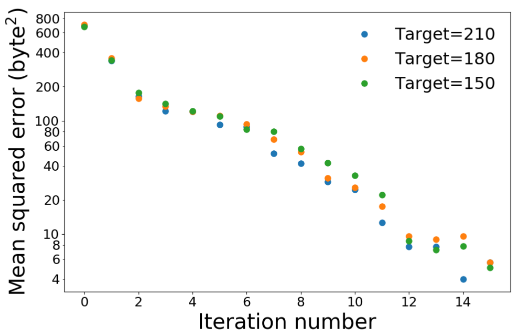

(e) λ= 100 pixels

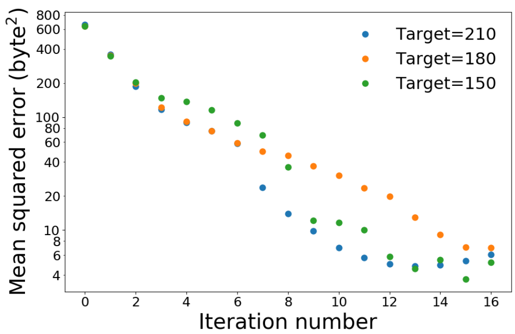

(f) λ= 150 pixels

Figure 25: Logarithmic display of the mean squared error progression during the iteration process for all displayed wavelengths. It is clearly visible that the error is decreasing with advanced iteration independent on what target intensity is used for the optimisation of the longer wavelengths. However, for the wavelengths of λ = 30 or 40 pixels, the lower target intensities seem to result in a smaller mean squared error. The measurements for the set with λ = 150 and a target intensity of 180 bytes diverges from the remaining measurements. After 10-12 iterations, the error does not change a lot and stays at a constant low level.

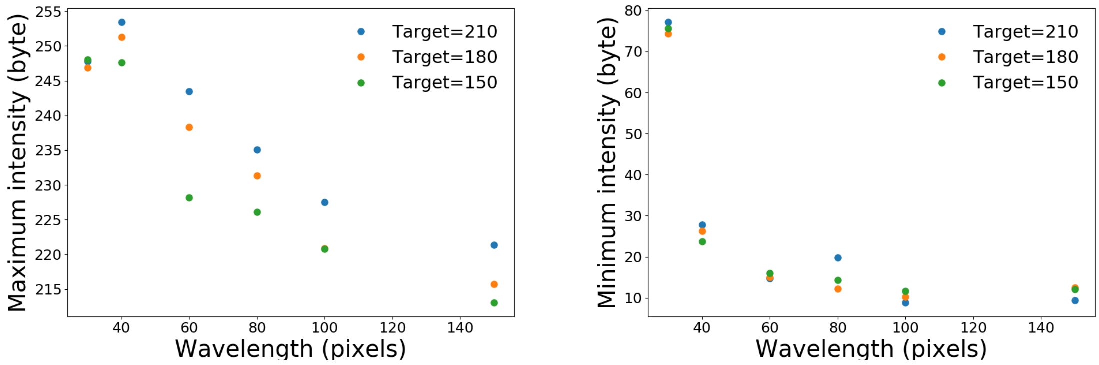

Figure 26: Maximum intensity (left) and offset intensity (right) as a function of the pattern wavelength. The offset is decreasing with increasing wavelength but is independent of the maximum target intensity. The maximum intensity is also decreasing with increasing wavelength but is dependent on the maximum target intensity. The higher the maximum target intensity, the higher is the actual reached value.

target. If the target intensity is higher, the final maximum intensity is also higher. This result is expected because the iteration error will be bigger if the target is set to a lower value so more mirrors will be turned off more quickly to reach the set target. Note that none of the iterations actually managed to reach the desired target value.

There are advantages in using both the higher target intensity and the lower target intensity values for the pattern optimisation. For a higher set target intensity, the overall final intensity will be higher, which means that a higher contrast between maximum and minimum is reached. However, when using small wavelengths the divergence to a perfect sinusoidal shape is higher for a higher target intensity, so the pattern displayed is not as homogeneous and accurate.

The results show that it is more difficult to optimise shorter wavelengths. This is visible in the increased variation from the actual target intensities and mean squared error for smaller wavelengths. Moreover, the measured images show that it is harder to reach a homogenous sinusoidal pattern for small wavelengths. This is due to the fact that fewer pixels are used to create a period and so fewer pixels can be turned off in the center of the peak to improve the pattern.

5.3.3 Arbitrary Pattern Optimisation

We finally want to show that we can display any kind of grey patterns after binarisation and pattern optimisation. In the last section, we already have proven that sinusoidal patterns can be binarised and optimised with a satisfying result. In order to show the same for arbitrary patterns, I used grey pictures of my advisors, as shown in Fig. 27, to be displayed with the DMD. These pictures were binarised and optimised using the same algorithm and settings as for the sinusoidal patterns. The result is shown in Fig. 27. The optimisation worked for the pictures of both supervisors. The effect was mostly to create a more homogenous intensity throughout the whole image area. However, a few of the sharp features are lost. This might be due to a calibration problem. The region of interest on the camera needs to be detected manually, and if the region is not found accurately, the resized measured image does not overlap perfectly with the target pattern. If the calibration is not sufficiently good, sharp features are lost in the optimisation process. The sinusoidal patterns are less sensitive to the calibration of the camera region of interest because the intensity varies only in the horizontal direction whereas the vertical direction consists of lines of equal intensity.

Figure 27: 8-bit grey pictures of my advisors Prof. Tilman Esslinger (top left) and Dr. Robert Smith (top right) and measured images of Rob and Tilman before (middle) and after optimisation with 10 iterations (bottom). The optimised pictures show a more homogenous intensity level but lose a few of the sharp features.

6 Switching Dynamics

In order to perform Bragg spectroscopy with a high excitation energy we need to switch between consecutive sinusoidal patterns quickly. The maximum available excitation energy depends on the maximum achievable refresh rate of the DMD divided by the number of frames per period. This shows that when a higher refresh rate is available, the same energy state can be excited using a higher number of frames and thereby creating a smoother transition. Next to the maximum refresh rate, the dynamics during a switch between frames is affecting the intensity of the light projected onto the atom plane. This chapter investigates the switching dynamics of the DMD to ensure a sufficiently fast and clean switching between the different sine frames.

6.1 Test Setup

The DMD can be operated in two different modes, the normal mode and the uninterrupted mode [42]. They affect the dynamics of the DMD during the switching period between consecutive frames.
The normal mode resets the mirrors to the ‘off’ state inbetween switches. The uninterrupted mode switches between the modes automatically without resetting to the parking state. During the switching, there is an inherent dark time where no light is reflected off the device. This might affect the Bragg excitation of the atoms if it is in the order of a few µs. Depending on the minimum dark time in the normal mode, one of the two modes might be more favourable for our purposes.
Additionally to the dark time, the mirrors oscillate around their default position after being switched back to the ‘On’ state. These lead to intensity fluctuations of the total intensity reflected into the ‘On’ state.
In order to investigate this behaviour, the light reflected off the DMD is focused onto a fast photodiode, depicted in Fig. 28. Two lenses are used because we want to capture as many

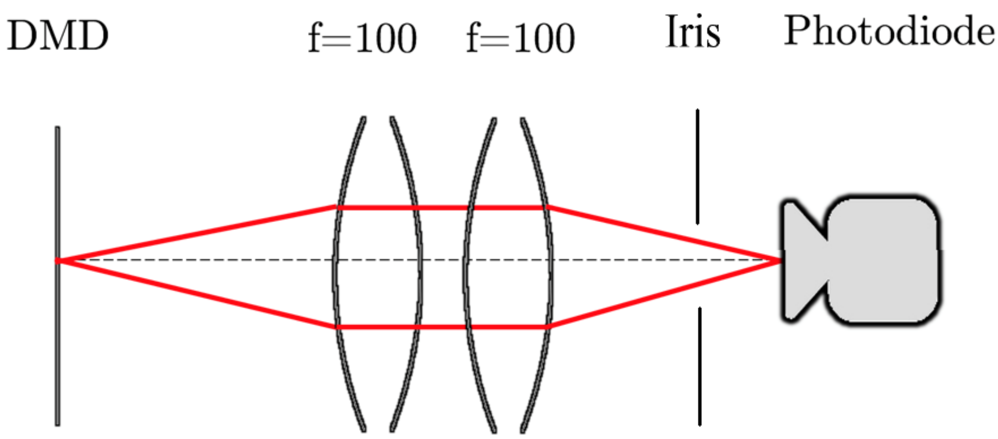

Figure 28: Setup for testing the switching dynamics of the DMD. The two lenses are necessary for efficient capturing of multiple reflected orders and focusing them onto the active area of the photodiode. Moreover, the aperture is closed to filter out higher diffraction orders for certain measurements. The graphic was created by my co-worker Alexander Norden.

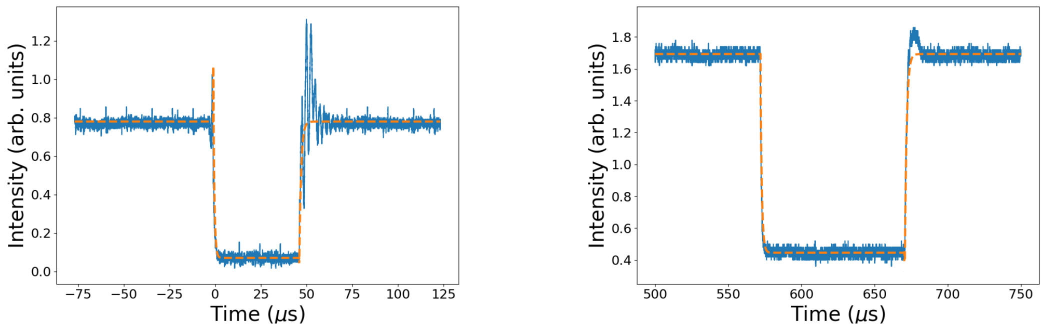

Figure 29: Normal mode switching with the V7001 model (left) and the V6501 model (right). At the beginning of a switch, the intensity drops to 0 with an exponential decay. After the minimum dark time, it rises to the normal mode intensity level with an exponential rise. The measurement on the left uses a repetition rate of 9 kHz whereas the measurement on the right uses a repition rate of 5 kHz. The decay and rise time as well as the minimum dark time were obtained with a fit to the data (orange curve). The V7001 model shows an oscillating behaviour during the intensity rise.

diffraction orders as possible. The different orders diverge a lot so we have to be as close to the DMD as the beam path allows us. The combination of two lenses provided the best focusing result. An additional aperture can be used to select only certain orders. The total intensity is monitored with a photodiode.
As mentioned in Sec. 3.5, we use two different DMD models in these measurements and compare the results of their switching dynamics.

6.2 Switching Dynamics Measurements

The switching dynamics of both models were tested. For this purpose, the light diffracted into the 0^{th} order as well as into higher orders was focused onto a photodiode. Two different operation modes were used, the **normal** and the **uninterrupted** mode.

6.2.1 Normal Mode

These measurements were done using only the 0^{th} order. To measure the switching dynamics in the normal mode, a combination of checked chess patterns and patterns with all pixels turned on were used.
In the normal mode, the screen resets to the 'off' direction between the pattern changes. There is a minimum time where the DMD is set to the 'off' direction before the new pattern is loaded. This is called the minimum dark time. The dark times were measured to be t_{dark} = 49 μs for the V7001 model and t_{dark} = 90 μs for the V6501 model, see Fig. 29. These values were obtained with a curve fit to the data and agree with the maximum frame rate of the two models (~ 22 kHz for V7001, ~ 10 kHz for V6501).
The recorded intensity shows an interesting behaviour. As soon as the mirrors are turned to the 'off' state during a frame change, the intensity drops to zero in a quick exponential decay (τ = 0.6 μs for V7001 model and τ = 0.95 μs for the V6501 model). When turning on the new pattern, the intensity rises exponentially to the level according to the number of

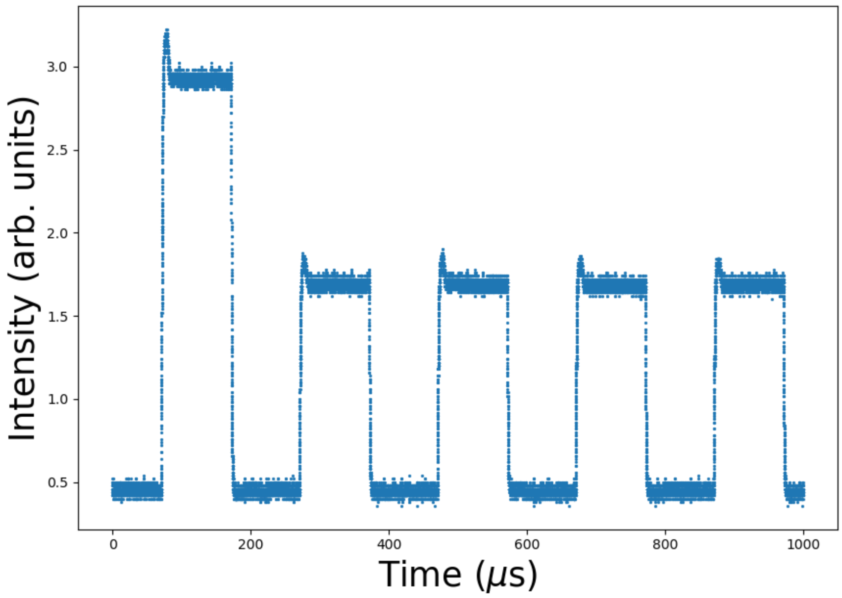

Figure 30: Switching in the normal mode of the V6501 model with a repetition rate of 5 kHz. For the measurement, a chess pattern in combination with 'all-on' pattern is used (higher intensity level). After a switch, the intensity rises to a higher level and decays to a lower constant intensity level.

pixels turned on in the corresponding pattern. The rise time were determined with a fit to be $\tau = 1$ µs for V7001 model and $\tau = 1.2$ µs for the V6501 model, see Fig. 29.
During the rise, the intensity overshoots to a higher lever and decays in a damped oscillation to a lower level. The overshoot is more prominent the more pixels are turned on to form that pattern (see 'all-on' pattern of V6501 measurement in comparison to half of the pixels turned on in chess pattern, Fig. 30). The damped oscillations are only observable for the V7001 model.
Due to the high dark time between consecutive frames, this mode is not suitable for performing Bragg spectroscopy.

6.2.2 Uninterrupted Mode

In the uninterrupted mode, the situation is more complicated. We choose a series of different patterns to investigate the situation in more detail, see Fig. 31.

V7001 Uninterrupted Mode Measurements
The first measurements were done with the V7001 model, where we only looked at the 0^{th} diffraction order:
We observed that between frame changes the intensity drops to zero. Moreover, when the pattern is changing during a frame change (for example switch from pattern 'a' to 'b'), there is a decay in intensity happening, see Fig. 32. This decay is not happening if the following pattern is the same as the currently displayed pattern.

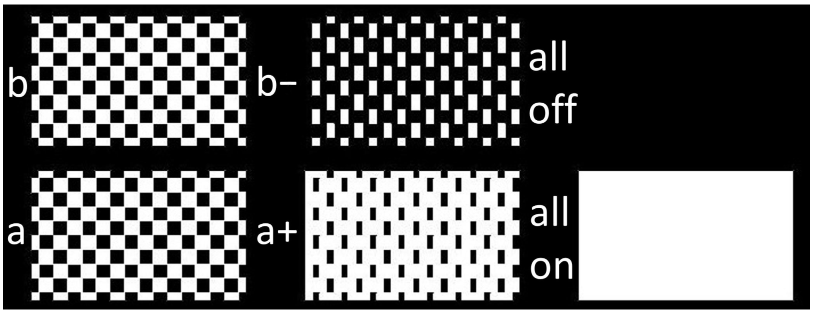

Figure 31: Variety of patterns used for testing the switching dynamics. The left column shows the normal checkerboard patterns, where the top one is an inverted version of the bottom one. We call these patterns ‘a’ and ‘b’. The middle column shows uneven checkerboard patterns. The bottom one is essentially pattern a with half the pixels from pattern ‘b’ also turned on. It is called ‘a+’. The top one is pattern b with half the pixels of pattern ‘b’ turned off. It is called ‘b-’. The right column shows all pixels turned on or all pixels turned off. They are called ‘all-on’ and ‘all-off’.

V6501 Uninterrupted Mode Measurements

We used the series of patterns displayed in Fig. 31 to understand in more depth what is happening during frame switches. We investigate the dynamics of light diffracted only in the 0^{th} order and into all orders together.

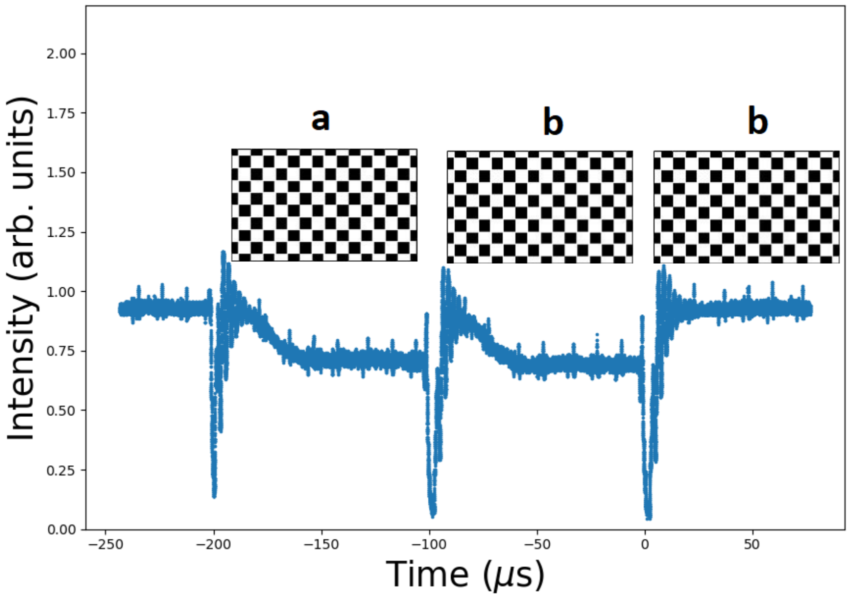

Figure 32: Example measurement V7001 model. The sequence ‘abb’ was used in the uninterrupted mode with a repetition rate of 10 kHz. A decay into a lower level is happening just before the frame changes from ‘a’ to ‘b’ and from ‘b’ to ‘a’ whereas when the frame changes from ‘b’ to ‘b’ no decay is visible.

All Order Dynamics
From the results observed with light diffracted into all orders we can see that during a frame change, first all pixels that have to be turned off are turned off and after that, new pixels forming the new pattern are turned on. Pixels that do not change position do not cause a change to the intensity diffracted into all orders (see Fig. 33).

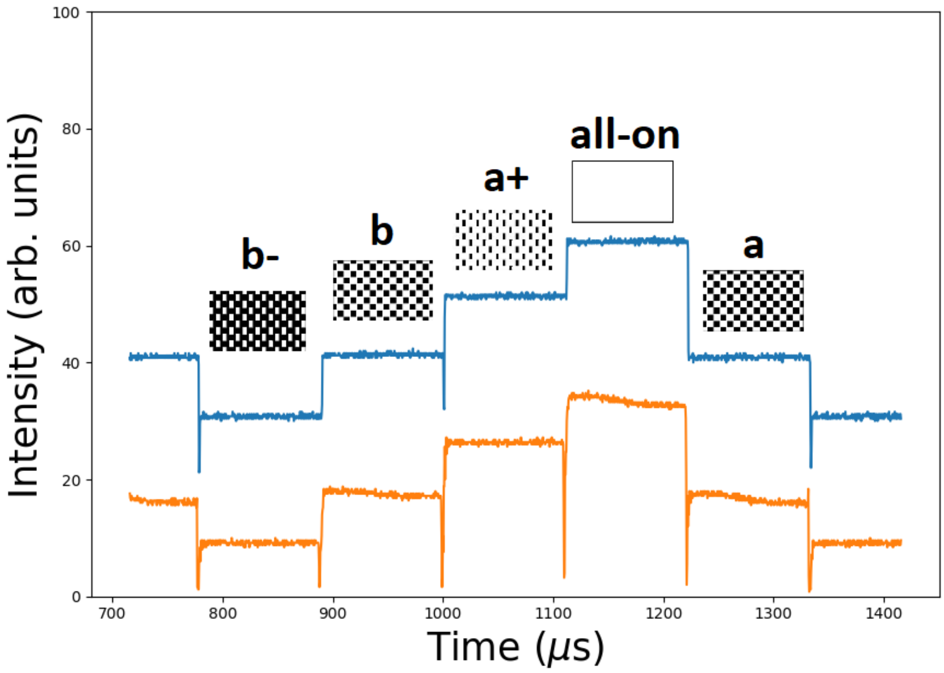

Figure 33: Intensity of all orders (blue) and only the 0^{th} order (orange) in uninterrupted mode of V6501 DMD, where an y-offset of 20 is introduced to the blue curve to increase the visibility. The sequence 'b- b a+ all-on a' with a repetition rate of 9 kHz is used.
During the frame changes from 'a' to 'b-', 'b' to 'a+' and 'all-on' to 'a' there are pixels that need to be turned off. This is displayed by an intensity drop in the blue curve. In the first two cases, there are new pixels turned on additionally, so there is a rise in intensity again after the drop. For the other pattern changes, only pixels are turned on so no intensity drop is seen in the blue curve.
For the orange curve, the intensity drops to zero during every frame change. If during the upcoming frame change pixels have to be turned off, the intensity of the current level will decay onto a lower value. This is the case for the changes from patterns 'a' to 'b-', 'b' to 'a+' and 'all-on' to 'a'.

Additionally to the pattern combination described in Fig. 33, we investigated all the different combinations of patterns and could verify the following rule for light diffracted in any of the orders.
Pattern changes that require certain pixels to turn off will turn off those pixels before turning on new pixels.

0^{th} Order Dynamics
The situation for light only diffracted into the 0^{th} order is different. Firstly, we always

observe a drop to zero intensity during a frame change. This implies that mirrors which are not turned off will slightly change the angle and thus not reflect into the 0^{th} order but higher orders during the pattern change. Secondly, whenever pixels are turned off in the upcoming pattern change, the intensity level will decay to a lower level before the change. This decay is proportional to the number of pixels being turned off in the pattern change. This decay is not seen when observing all the orders together so the light that is not diffracted into the 0^{th} order will be diffracted into higher orders instead, see Fig. 33.
An explanation for this behaviour is that pixels which are about to be turned off in the upcoming frame change are 'prepared' and their reflection angle is changed slightly such that a percentage of the light reflected of those mirrors is now diffracted into higher orders instead. 'Preparation' means, that the spring bringing the pixels into position is already imposed with a force before the position change is happening. A group at the University of Cambridge observed a similar behaviour with their DMD model V7001 [38]. In both cases, the decay is more prominent when a lot of pixels are changed, but is less observable if only a few numbers of pixels are changed, which confirms our assumption about the pixel 'preparation'.
The flickering of the mirrors during a pattern change will most likely not affect the atoms since the pattern change is happening in timescales well below 2 μs. The gradual decay to a lower intensity level, however, is problematic because it results in a varying intensity of light. For the case of a slowly translating sinusoidal pattern, it will not affect the experiment a lot because only few pixels are changed per translation step. Moreover, one could optimise the greyscaling algorithm to minimise the number of pixels that need to be changed.

Finally, we compare the behaviour of the two DMD models in the uninterrupted mode. They behaved very similarly, although the V6501 model showed less oscillating behaviour during the decay and the intensity level was less noisy. However, the maximum switching rate is significantly larger for the V7001 model. In this case, operation with a high switching rates is not desirable because the oscillating behaviour in combination with the intensity decay will affect the atoms more with more frequent pattern changes.
The V6501 model is more favourable, because the oscillating behaviour is not observed, so it can be operated at its maximum switching rate and enable a higher number of frames per translation period. Assuming a maximum excitation energy of $\omega = 2\pi \cdot 512$ Hz and operation at the maximum switching rate would allow for a very high number of frames per period of $N = 20$. This is higher than what is needed for a smooth transition so we can assume to access higher excitation energies than used in the Innsbruck experiment [33].

7 Conclusions and Outlook

7.1 Conclusions

The work undertaken over the course of this thesis has laid the foundation for performing Bragg spectroscopy on a dipolar quantum gas of erbium atoms using a DMD. The DMD is used to generate sinusoidal lattice potentials that are projected onto the atoms via an imaging setup.

In particular, we prepared an imaging setup for the direct projection method with a theoretical target resolution of 2.1 μm. The imaging setup consists of a two-stage demagnification setup using two telescopes where in the second telescope the last lens is replaced with a custom-built objective to account for aberrations. The resulting demagnification factor is 83 and allows a high number of DMD pixels to be projected on a small area to enable a high level of greyscaling.

The resolution of the imaging setup was measured in two steps. First, the objective's resolution was measured using a test slide of lines with known linewidths and a lower bound for the resolution of 2.18 ± 0.19 μm was found. The second test determined the resolution of the second telescope of the imaging system and delivered a result of 2.55 ± 0.12 μm. The result is taken as an upper bound to what our actual imaging resolution is and could possibly be improved by magnifiying the projected image to avoid measuring the resolution in the atom plane directly. This would prevent being limited by the camera pixel size.

In addition to determining the boundaries of our imaging system, we confirmed that sinusoidal patterns with wavelengths as low as 15.2 μm can be projected onto the atom plane and resemble the desired sinusoidal pattern accurately through employing a pattern correction algorithm. The Floyd-Steinberg algorithm was used to minimise the error in pattern binarisation which is enabled by our high level of greyscaling. Additionaly, a pattern correction algorithm was developed that allows for the iterative improvement of the projected patterns. A good set of iteration parameters for pattern correction were found. Moreover, we identified longer wavelengths to be more handy in the correction process because more pixels generate one period in the pattern which allows for finer tuning in the correction process. In order to project and optimise sinusoidal patterns with smaller wavelengths, an additional magnification system is required.

Lastly, we investigated the switching dynamics of two DMD models. Two different operational modes were tested, namely the normal mode and the uninterrupted mode. The normal mode is unsuitable for Bragg spectroscopy measurements due to its long dark time. Switching in the uninterrupted mode resulted in dark times lower than 2 μs which is sufficiently low for this purpose. Both models showed a special behaviour for pattern changes that require many pixels to switch state, which was identified by observing the intensity diffracted into the 0^{th} order and higher orders. A decay of 0^{th} order intensity is occuring during the projection time before the pattern change happens, proportional to the number of pixels switching position. The V7001 model showed additional oscillations during pattern changes which proved the V6501 model to be more suitable for the Bragg spectroscopy measurements. Bragg spectroscopy will not require many pixels to change simultaneously, so the intensity decay will not be significant. The required maximum switching rate for Bragg spectroscopy is complied by both models and allows for smooth pattern transitions.

7.2 Outlook

The setup is completed and can in principle be used to perform Bragg spectroscopy. There are a few further tests that would confirm the presented results.
First, we need to design and build a magnifying imaging system which would allow more precise measurements of the resolution. This enables projecting and measuring sinusoidal potentials with a wavelength equal to the resolution in the atom plane and provide a more definite number for the resolution of the imaging setup. Such a magnification setup would require either a second objective or more advanced lenses, so as not to introduce aberrations or worsen the resolution and thereby falsify the results.
The next step would be to build an imaging setup for the holographic projection method. The setup will consist of a magnifying telescope and the existing objective. It is useful to compare the two projection methods and their corresponding maximum achievable resolution to estimate the maximum available momentum transfer for Bragg spectroscopy.
In the near future, the setup can be implemented with the real experiment to measure the dispersion relation of a dipolar quantum gas in a uniform 2D potential. The setup in the experiment involves a few steps including the implementation of the DMD regulation with the sequence used to control the experiment. Then, for each momentum that should be probed, the pattern correction algorithm has to be employed first before performing the Bragg spectroscopy. Moreover, there are geometrical constraints that need to be considered carefully because multiple laser systems need access to the science chamber. A solution might be to combine those systems with the 583 nm laser of the Bragg spectroscopy setup and project them onto the atoms together using the objective.

8 Acknowledgements

This work was conducted at the Physics Department of the University of Oxford. A lot of people were involved to make this project and exchange possible to whom I am very grateful.
First of all, I would like to thank my supervisor from my home institution ETH Zürich, Prof. Tilman Esslinger for giving me the great opportunity to conduct my Master's thesis as part of his Quantum Optics group and enabling the exchange with the University of Oxford. Moreover, I would like to thank Tilman for his enthusiastic lectures in quantum optics and quantum gases through which I could develop a broader understanding in the field of ultracold atoms.
Secondly, I would like to express gratitude to my supervisor in Oxford, Dr. Rob Smith. Thank you for assisting with the organisation of the exchange as well as answering a lot of theoretical and practical questions. You always had an open door and not only responded to questions and problems but also encouraged new ways to think about physics.
I am very grateful for my colleague in this project, Milan Krstajić. Not only does he have an astonishing talent for experimental work, but also proved a good sense of humour and creativity in approaching challenges. Thank you for your endless patience in enduring my questions and for guiding me through this project.
Also, I would like to thank my co-worker Alexander Norden. It was a pleasure to work with you and dive deeper into the world of optics.
Further, I would like to express my gratitude to all the group members of the dipolar quantum gases group in Oxford: Dr. Anna Marchant, Peter Juhász and Lucas Hofer. You made me feel very welcome in Oxford and were very supportive throughout this project.
Lastly, I would like to thank the QSIT program fom the national centre of competence in research for their generous support given through the INSPIRE potentials award.

Eidgenössische Technische Hochschule Zürich
Swiss Federal Institute of Technology Zurich

Declaration of originality

The signed declaration of originality is a component of every semester paper, Bachelor's thesis, Master's thesis and any other degree paper undertaken during the course of studies, including the respective electronic versions.

Lecturers may also require a declaration of originality for other written papers compiled for their courses.

I hereby confirm that I am the sole author of the written work here enclosed and that I have compiled it in my own words. Parts excepted are corrections of form and content by the supervisor.

Title of work (in block letters):

Generation of Bragg Spectroscopy Potentials with a DMD

Authored by (in block letters):
For papers written by groups the names of all authors are required.

Name(s):	**First name(s):**
Clausen	Gloria

With my signature I confirm that

- I have committed none of the forms of plagiarism described in the 'Citation etiquette' information sheet.
- I have documented all methods, data and processes truthfully.
- I have not manipulated any data.
- I have mentioned all persons who were significant facilitators of the work.

I am aware that the work may be screened electronically for plagiarism.

Place, date
Grönwohld, 23 April 2020

Signature(s)
Gloria Clausen

For papers written by groups the names of all authors are required. Their signatures collectively guarantee the entire content of the written paper.

A Appendix

A.1 DMD Technical Data

Model	V-7001	V6501
Micromirrors	1024 x 768	1920 x 1080
Micromirror Pitch	13.7 µm	7.6 µm
Active Area	14 mm x 10.5 mm	14.5 mm x 8.2 mm
max. Switching rate	22.7 kHz	10.3 kHz

Table 3: Overview of technical data of the two DMD devices.

A.2 Floyd-Steinberg Error Diffusion Algorithm

The Floyd-Steinberg error diffusion algorithm to binarise an image called I_{orig} is given by:

```
def floyd_steinberg(orig_img):
    out_img=np.copy(orig_img)
    for i in range image_height:
        for j in range image_width:
            oldpixel  = orig_img[i,j]
            newpixel  = round(oldpixel)
            out_img[i,j]  = newpixel
            err  = oldpixel - newpixel
            orig_img[i, j+1] = orig_img[i, j+1] + err * 7 / 16
            orig_img[i+1,j-1] = orig_img[i+1, j-1] + err * 3 / 16
            orig_img[i+1, j] = orig_img[i+1, j] + err * 5 / 16
            orig_img[i+1, j+1] = orig_img[i+1, j+1] + err * 1 / 16
            return (out_img)
```

A.3 Pattern Correction Algorithm

The algorithm used for the pattern correction is given by:

```
I_old=I_targ;
for i=1:iter_num
    I_meas = imresize(I_meas, [1920 1080]);
    if i>1
        I_old=_I_new;
    I_err=255*tanh(5/255*(I_meas/sum(sum(I_meas))
        *sum(sum(I_corr))-I_corr));
    I_new=I_old-m*I_err;
    I_bin=FloydSteinberg(I_new);
```

Here, *m* is the error adding factor and iter_num is the number of iterations.

A.4 Resolution Measurements

A.4.1 Test Target Measurements

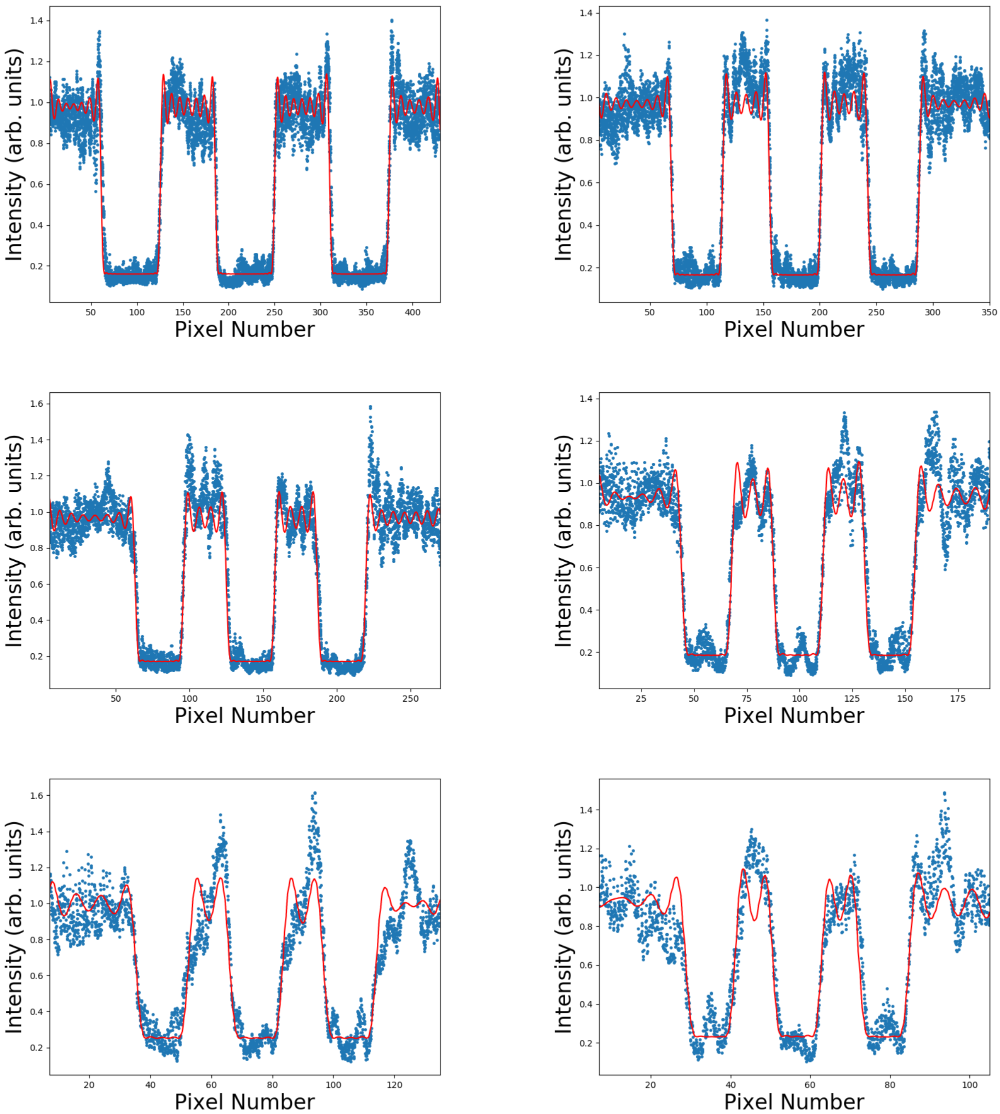

Figure 34: Resolution measurements using the test target. The linewidths shown in the graphs are 31.3 µm, 25 µm, 17.9 µm, 12.5 µm, 8.9 µm and 6.3 µm from left top to right bottom.

A.4.2 DMD Measurements

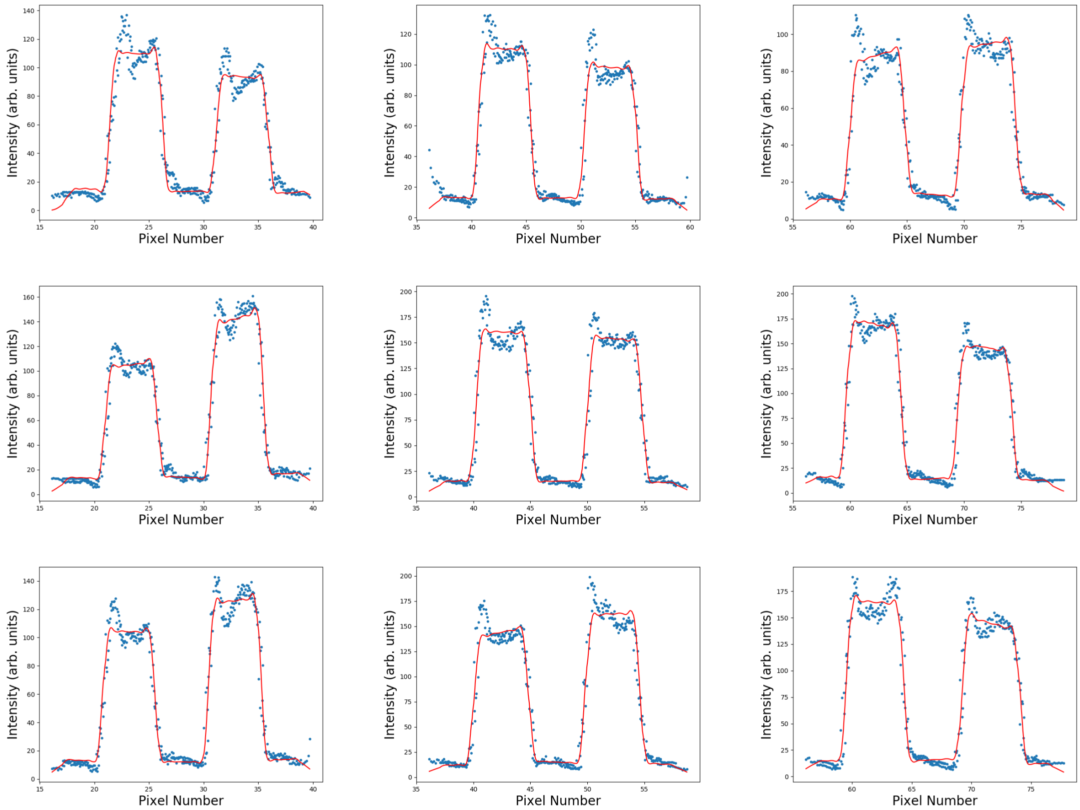

Figure 35: Resolution measurements using the DMD. The fits of two DMD lines to Eq. 37 are shown. The fits correspond to the upper left region to the bottom right region, as indicated by their position in the figure.

References

[1] ABUELMA'ATTI, M. Trigonometric approximations for some bessel functions. *Active and Passive Electronic Components 22* (1999).

[2] AIKAWA, K., FRISCH, A., MARK, M., BAIER, S., RIETZLER, A., GRIMM, R., AND FERLAINO, F. Bose-Einstein Condensation of Erbium. *Phys. Rev. Lett. 108* (May 2012).

[3] AIRY, G. B. On the Diffraction of an Object-glass with Circular Aperture. *Transactions of the Cambridge Philosophical Society 5* (Jan. 1835).

[4] ALT, W. An objective lens for efficient fluorescence detection of single atoms. *Optik 113*, 3 (2002).

[5] ANDERSON, M. H., ENSHER, J. R., MATTHEWS, M. R., WIEMAN, C. E., AND CORNELL, E. A. Observation of Bose-Einstein Condensation in a Dilute Atomic Vapor. *Science 269*, 5221 (1995).

[6] ANDREWS, M. R., TOWNSEND, C. G., MIESNER, H.-J., DURFEE, D. S., KURN, D. M., AND KETTERLE, W. Observation of Interference Between Two Bose Condensates. *Science 275*, 5300 (1997).

[7] BAN, H. Y., JACKA, M., HANSSEN, J. L., READER, J., AND MCCLELLAND, J. J. Laser cooling transitions in atomic erbium. *Opt. Express 13*, 8 (Apr 2005).

[8] BLOCH, I., HÄNSCH, T. W., AND ESSLINGER, T. Atom Laser with a cw Output Coupler. *Phys. Rev. Lett. 82* (Apr 1999).

[9] BLOCH, I., HÄNSCH, T. W., AND ESSLINGER, T. Measurement of the spatial coherence of a trapped Bose gas at the phase transition. *Nature 403*, 6766 (Jan. 2000).

[10] BRION, E., PEDERSEN, L. H., AND MOLMER, K. Adiabatic elimination in a lambda system. *Journal of Physics A: Mathematical and Theoretical 40*, 5 (Feb. 2007).

[11] CHOMAZ, L., VAN BIJNEN, R. M. W., PETTER, D., FARAONI, G., BAIER, S., BECHER, J. H., MARK, M. J., WÄCHTLER, F., SANTOS, L., AND FERLAINO, F. Observation of roton mode population in a dipolar quantum gas. *Nature Physics 14*, 5 (May 2018).

[12] DAVIS, K. B., MEWES, M. O., ANDREWS, M. R., VAN DRUTEN, N. J., DURFEE, D. S., KURN, D. M., AND KETTERLE, W. Bose-Einstein Condensation in a Gas of Sodium Atoms. *Phys. Rev. Lett. 75* (Nov 1995).

[13] DE LAETER, J. R., BÖHLKE, J. K., BIÈVRE, P. D., HIDAKA, H., PEISER, H. S., ROSMAN, K. J. R., AND TAYLOR, P. D. P. Atomic weights of the elements. Review 2000 (IUPAC Technical Report). *Pure and Applied Chemistry 75*, 6 (2003).

[14] ENGHAG, P. *Encyclopedia of the Elements: Technical Data - History - Processing - Applications*. Wiley, 2008.

[15] Floyd, R. W., and Steinberg, L. An Adaptive Algorithm for Spatial Greyscale. *Proceedings of the Society for Information Display 17*, 2 (1976).

[16] Foot, C. J. *Atomic physics*. Oxford master series in atomic, optical and laser physics. Oxford University Press, Oxford, 2007.

[17] Frisch, A., Aikawa, K., Rietzler, A., Schindler, J., Zupanic, E., Grimm, R., and Ferlaino, F. Narrow-line magneto-optical trap for erbium. *Physical Review A 85* (05 2012).

[18] Goodman, J. W. Introduction to Fourier optics. *Introduction to Fourier optics, 3rd ed., by JW Goodman. Englewood, CO: Roberts & Co. Publishers, 2005 1* (2005).

[19] Gotlibovych, I. *Degenerate Bose Gases in a Uniform Potential* . PhD thesis, University of Cambridge, 2014.

[20] Griesmaier, A., Werner, J., Hensler, S., Stuhler, J., and Pfau, T. Bose-Einstein Condensation of Chromium. *Phys. Rev. Lett. 94* (Apr 2005).

[21] Ha, L.-C., Clark, L. W., Parker, C. V., Anderson, B. M., and Chin, C. Roton-Maxon Excitation Spectrum of Bose Condensates in a Shaken Optical Lattice. *Physical Review Letters 114*, 5 (Feb. 2015).

[22] Hartog, E. A. D., Chisholm, J. P., and Lawler, J. E. Radiative lifetimes of neutral erbium. *Journal of Physics B: Atomic, Molecular and Optical Physics 43*, 15 (July 2010).

[23] Juhász, P. Optical trapping and transport of ultracold erbium atoms, First year report. *University of Oxford* (2019).

[24] Klein, M., and Furtak, T. *Optics*. Wiley series in pure and applied optics. Wiley, 1986.

[25] Krstajic, M. Arbitrary Dynamical Potentials for Ultracold Atoms . Master's thesis, University of Cambridge, 2017.

[26] Krstajic, M. Erbium BEC in an Optical Box, First year report. *University of Cambridge* (2018).

[27] Landau, L. On the theory of superfluidity of helium II. *Journal of Physics (Moscow) 11*, 25 (1947).

[28] Letokhov, V., Minogin, V., and Pavlik, B. Cooling and capture of atoms and molecules by a resonant light field. *Soviet Journal of Experimental and Theoretical Physics 45* (03 1977).

[29] Lu, M., Burdick, N. Q., Youn, S. H., and Lev, B. L. Strongly Dipolar Bose-Einstein Condensate of Dysprosium. *Phys. Rev. Lett. 107* (Oct 2011).

[30] Madison, K. W., Chevy, F., Wohlleben, W., and Dalibard, J. Vortex Formation in a Stirred Bose-Einstein Condensate. *Phys. Rev. Lett. 84* (Jan 2000).

[31] Matthews, M. R., Anderson, B. P., Haljan, P. C., Hall, D. S., Wieman, C. E., and Cornell, E. A. Vortices in a Bose-Einstein Condensate. *Phys. Rev. Lett. 83* (Sep 1999).

[32] Perego, E. Generation of arbitrary optical potentials for atomic physics experiments using a Digital Micromirror Device. Master's thesis, University of Florence, 2015.

[33] Petter, D., Natale, G., van Bijnen, R. M. W., Patscheider, A., Mark, M. J., Chomaz, L., and Ferlaino, F. Probing the Roton Excitation Spectrum of a Stable Dipolar Bose Gas. *Phys. Rev. Lett. 122* (May 2019).

[34] Petter, D., Natale, G., van Bijnen, R. M. W., Patscheider, A., Mark, M. J., Chomaz, L., and Ferlaino, F. Supplemental Material: Probing the roton excitation spectrum of a stable dipolar Bose gas. *Phys. Rev. Lett. 122* (May 2019).

[35] Reiter, F., and Sørensen, A. S. Effective operator formalism for open quantum systems. *Phys. Rev. A 85* (Mar 2012).

[36] Saleh, B. E., and Teich, M. C. *Fundamentals of photonics*. John Wiley & Sons, 2019.

[37] Santos, L., Shlyapnikov, G. V., and Lewenstein, M. Roton-Maxon Spectrum and Stability of Trapped Dipolar Bose-Einstein Condensates. *Physical Review Letters 90*, 25 (Jun 2003).

[38] Schmitt, J., and Galka, M. Private Communication. *University of Cambridge* (2020).

[39] Steck, D. A. Quantum and Atom Optics, lecture notes. *University of Oregon* (2006).

[40] Steinhauer, J., Ozeri, R., Katz, N., and Davidson, N. Excitation Spectrum of a Bose-Einstein Condensate. *Phys. Rev. Lett. 88* (Mar 2002).

[41] Stenger, J., Inouye, S., Chikkatur, A. P., Stamper-Kurn, D. M., Pritchard, D. E., and Ketterle, W. Bragg Spectroscopy of a Bose-Einstein Condensate. *Physical Review Letters 82*, 23 (Jun 1999).

[42] Texas Instruments. DLP6500 0.65 1080p MVSP Type A DMD datasheet (Rev. A). *http://www.ti.com/lit/ds/symlink/dlp6500flq.pdf* (October 2018).

[43] Zupancic, P. Dynamic holography and beamshaping using digital micromirror devices. Master's thesis, Ludwig-Maximilians-Universität München, 2013.